Atmospheric Environment 343 (2025) 120951

Contents lists available at ScienceDirect

Atmospheric Environment

journal homepage: www.elsevier.com/locate/atmosenv

Explainable hybrid deep learning framework for enhancing multi-step solar ultraviolet-B radiation predictions

Salvin S. Prasad [a,b], Lionel P. Joseph [b], Sujan Ghimire [b], Ravinesh C. Deo [b,*], Nathan J. Downs [b], Rajendra Acharya [b], Zaher M. Yaseen [c]

[a] School of Sciences, College of Engineering, and Technical Vocational Education and Training, Fiji National University, Samabula, Suva, Fiji
[b] School of Mathematics, Physics and Computing, University of Southern Queensland, Toowoomba, QLD 4350, Australia
[c] Civil and Environmental Engineering Department, King Fahd University of Petroleum and Minerals, Dhahran, 31261, Saudi Arabia

HIGHLIGHTS

- Explainable hybrid system is developed to forecast ultraviolet-B radiation at multi-step horizons.
- Explainable artificial intelligence (*xAI*) explains physical interpretations of model prediction outcomes.
- Optuna and RFECV feature selection optimizes predictive performance of *xAI* model.
- *xAI* provides ultraviolet-B exposure information to help mitigate detrimental UV exposure effects.

GRAPHICAL ABSTRACT

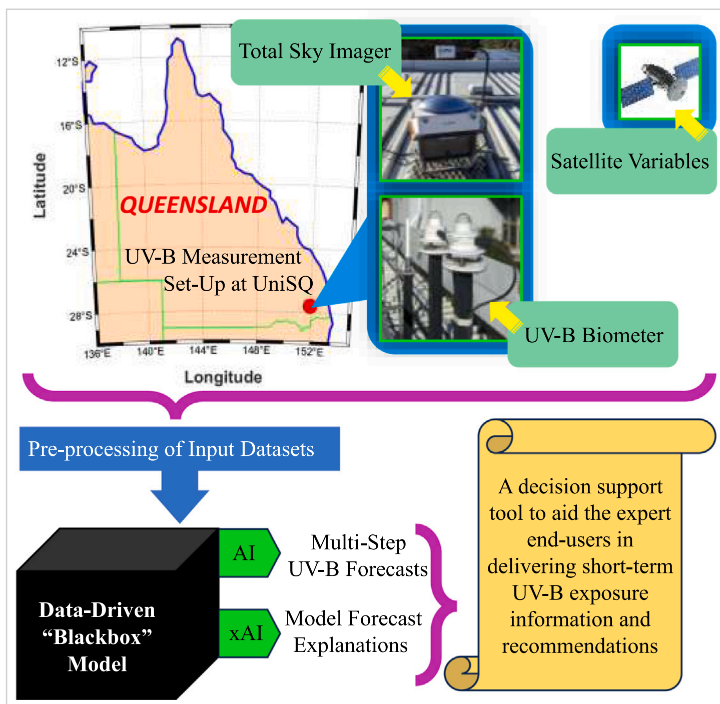

ARTICLE INFO

MSC:
0000

ABSTRACT

Acute exposure effects of short-wavelength solar ultraviolet-B (*UV-B*) radiation can trigger skin-based diseases and eye health ailments in humans and animals, as well as disrupt photosynthetic or hormonal systems in plants. Within the *UV* wavebands, high levels of *UV-B* exposure are particularly severe and the leading cause

* Corresponding author.
E-mail addresses: salvin.prasad@fnu.ac.fj (S.S. Prasad), lionel.joseph@usq.edu.au (L.P. Joseph), sujan.ghimire@unisq.edu.au (S. Ghimire), ravinesh.deo@usq.edu.au (R.C. Deo), nathan.downs@usq.edu.au (N.J. Downs), rajendra.acharya@unisq.edu.au (R. Acharya), Zaheryaseen88@gmzail.com, z.yaseen@kfupm.edu.sa (Z.M. Yaseen).

https://doi.org/10.1016/j.atmosenv.2024.120951
Received 7 August 2024; Received in revised form 5 November 2024; Accepted 25 November 2024
Available online 4 December 2024
1352-2310/

1111
Keywords:
Ultraviolet-B radiation forecasting
Optuna optimization
Deep learning
TabNet
"black-box" model
Explainable artificial intelligence (*xAI*)

of skin cancers. Therefore, accurate and explainable short-term *UV-B* forecasts are essential for effectively providing sun exposure information to the public and *UV* experts. To address this pressing issue, we developed an explainable hybrid TabNet framework optimized with the Optuna algorithm. The model was trained using predictors derived from satellite products and sky images for the experimental site in Toowoomba, Queensland, Australia. For model training, 3,863 data points were utilized from July 1, 2002 to February 29, 2004. The model development phase entailed dimensionality reduction using recursive feature elimination with cross-validation (RFECV) and principal component analysis (PCA) methods. The proposed model outperformed all competing counterparts, achieving comparatively high correlation coefficients of 0.908, 0.880, 0.868, and 0.868 for hourly, 2-hourly, 3-hourly, and 4-hourly forecast horizons, respectively. Explainable artificial intelligence (*xAI*) results, based on Local Interpretable Model-Agnostic Explanations (LIME) and Shapley Additive Explanations (SHAP), indicate that the antecedent lagged memory of *UV-B* radiation and the solar zenith angle contribute significantly to *UV-B* predictions. Ozone effects and cloud cover conditions are also influential features in this respect. The superior capabilities of the newly designed hybrid explainable TabNet model affirm its potential for *UV-B* monitoring and mitigating the harmful sun exposure risks for the public and terrestrial life.

1. Introduction

The ultraviolet (UV) region (200–400 nm) of the solar radiation waveband is an important environmental factor that poses both a beneficial and potentially harmful influence to plant, animal and human life. In humans, sufficient UV exposure facilitates the production of vitamin D to help maintain strong bones, muscles and autoimmune function (Coussens et al., 2017). Conversely, excessive UV exposure can cause sun burn, damage to DNA structure and skin cancer. These cancers include melanoma and non-melanoma (keratinocyte) skin cancers (Webb et al., 2016). Annually, around 7.7 million cases of non-melanoma skin cancer and 310,000 cases of malignant melanoma are reported worldwide (Sharaf et al., 2021; Cherrie and Cherrie, 2022). In addition, a global skin-cancer-led mortality rate of 126,000 was reported in 2018, where the majority of cases were recorded by nations located in temperate latitudes (Parker, 2021). Skin cancers of both types impose a significant economic burden on healthcare systems (Gordon and Rowell, 2015; Gordon et al., 2022), as well as challenges for the families of individuals suffering from the disease. In the case of animals, excessive sun exposure can trigger skin lesions, optical tumors, and at times fatality (Olarte Saucedo et al., 2019). In plants, solar radiation is a fundamental input to support photosynthetic reactions. However, these processes can be affected by irreversible or temporary damage when the plant cells are exposed to elevated UV radiation (Piri et al., 2011).

The Surface level UV spectrum, divided between the long wavelength *UV-A* (320−400 nm) and short wavelength *UV-B* (280–320 nm) are responsible for the aforementioned harmful exposure effects. Among the two components, the short wavelength *UV-B* radiation poses higher exposure severity than the *UV-A* (De Gruijl, 2002; Sterenborg and VanDerLeun, 1987). Though the *UV-A* waveband is a predominant component of the solar UV spectrum, it is associated with premature ageing and wrinkling of the skin (Matsumura and Ananthaswamy, 2004). However, *UV-B* exposure and the acute effects of exposure to *UV-B* including sun burn are closely associated with skin cancers and eye health ailments including cortical cataract and pterygium (Sterenborg and VanDerLeun, 1987; Cullen, 2011). In comparison with exposure to *UV-A*, *UV-B* exposure stimulates substantial stress in plants and poses detrimental effects on the genetic system and cell membranes (Csintalan et al., 2001). Further comparisons reveal that excessive exposure to *UV-B* damages the plant DNA, causing photosynthetic or hormone systems disorders (Hollósy, 2002). Overall, the *UV-B* waveband within the solar *UV* spectrum alone entails several harmful effects on the terrestrial environment, thus necessitating its efficient monitoring and exploration.

The incoming *UV* radiation, particularly the *UV-B* component is significantly modulated by some dominant environmental factors that include cloud cover conditions, ozone concentration, aerosol effects, dust scattering, precipitation and solar zenith angle (SZA) (Prasad et al., 2023; Ahmed et al., 2022). Among these parameters, SZA is predictable for each year, while the other variables can be forecast. However, cloud cover effects are significantly stochastic and are known to attenuate the ground transferring solar *UV-B* radiation. Due to its complex intermittent nature, partial cloud cover conditions can scatter the incoming *UV* waveband into harmful spikes that sometimes exceed nominal cloud-free levels (Prasad et al., 2024). In such a scenario, exposure to sudden escalated magnitudes of *UV-B* radiation can increase the risk of damage (Feister et al., 2015). Efficient dissemination of information regarding the severity level of the aforementioned *UV-B*-exposure-related damaging effects is highly important. However, there is no such threshold value that can be implemented to serve this purpose, as these damaging effects are led by cumulative exposure to *UV-B* radiation (Lavker et al., 1995). In this regard, short-term forecasts of cloud-affected *UV-B* radiation, capable of capturing deleterious high magnitudes of *UV-B* spikes can deliver more meaningful exposure risk information. To address this need, our study developed a predictive framework that forecasts short-term cloud-influenced *UV-B* radiation at multi-step horizons.

Initially, measurements of *UV-B* radiation were mostly achieved using ground-based monitoring systems, satellite instrumentation and empirical models (Bilbao and Miguel, 2013; Singh et al., 2018). In this respect, measurement instruments including scanning spectroradiometers require careful attention to ensure correct installation, as well as ongoing calibration and maintenance costs (Deo et al., 2017a). Remote and mountainous terrains also bring about additional challenges. Moreover, empirical models may necessitate extensive bias corrections resulting from the uncertainties induced by the impact of numerous climatic factors such as clouds, aerosol and ozone effects on solar radiation (Ahmed et al., 2022). Concurrently, conventional process-based mechanistic models and empirical models challenged by shot-term fluctuations and the non-linearity and of the data. Thus, the critical limitations and constraints observed in the aforementioned predictive methods have prompted the quest for more robust technologies that can learn and adapt to short-term changes in the atmospheric parameters that affect surface levels of *UV*.

Artificial intelligence (AI) powered frameworks such as machine learning (ML) and deep learning (DL) technologies can aid this purpose as AI predictive tools are readily accessible and can demonstrate a high level of robustness and cost-effectiveness over the long-term (Sardashti and Nazari, 2023). Technological advancement has enabled researchers to continually design many AI-inspired predictive systems with significant boosts in computational efficiency. However, to the best of the authors' knowledge, previous studies have not yet developed any ML or DL predictive models to predict short-term changes in the solar *UV-B*. Embracing this notion, our further discussion on related works will be confined to designing robust AI-inspired frameworks to forecast some critical wavebands of the ground-level solar radiation. In this regard, relevance can be drawn from some previous studies that integrated robust ML and DL predictive systems to effectively forecast solar photosynthetic-active radiation (Deo et al., 2022), solar *UV-A* radiation (Prasad et al., 2024), and the solar UV index (*UVI*) (Prasad et al., 2022). These studies and a number of other related research works, have provided valuable insights into understanding the architectural design of some robust AI tools displaying enhanced forecasting capabilities.

Consistent with several prior research works, the early deployment of AI-based predictive tools was accomplished using data-driven ML methods that are simple to implement and impose minimal computational burden. These ML methods are capable of mapping the non-linear data without explicit programming and do not require any extensive process-based cognition (Pal and Sharma, 2021; Qing and Niu, 2018). Artificial neural network (ANN) is one of the common ML algorithms that display better self-learning capability and high predictive accuracy in the domain of forecasting solar radiation. For instance, ANNs trained on diverse datasets have shown superior solar radiation forecasting skills at different forecast horizons in a number of countries that include Algeria and France (Notton et al., 2019), Australia (Ghimire et al., 2019), Italy (Alsina et al., 2016), Nigeria (Ozoegwu, 2019), Turkey (Ozgoren et al., 2012) and India (Premalatha et al., 2018). On the same platform, the tree-based models like random forest (RF) (Villegas-Mier et al., 2022) and gradient boosting-based models like XGBoost (XGB) (Huang et al., 2021) have also demonstrated elevated predictive performances at different forecast horizons and locations. Separate studies have demonstrated the utility of support vector regression (SVR) (Fan et al., 2020) and multivariate adaptive regression splines (MARS) (Balalla et al., 2021) in forecasting solar irradiance. Despite notable progress, standalone ML algorithms have been hampered by certain flaws. As an example, although SVR model efficiently often achieves global optimum convergence, the computational and memory demands hinder its scalability for large volumes of data (Santamaría-Bonfil et al., 2016). In applications with large datasets, tree-based models, known for their outlier sensitivity, can generate an excessive number of nodes from one tree and result in overfitting (Joseph et al., 2024a). During the training process, neural network-based models like ANN frequently become stuck in local minima and fail to find the global minimum of the loss function (Abdolrasol et al., 2021). However, the emergence of ANN facilitated a transition from traditional mathematical methods and linear ML algorithms to a more advanced DL approach (Brahma et al., 2015), capable of capturing complex underlying patterns in large datasets.

DL models have gained widespread acceptance for efficiently handling time-series data across diverse applications. Owing to their enhanced predictive capabilities, numerous climatic and atmospheric domains have shown increased interest in using the hybridized version of these DL predictive tools (Sharma et al., 2022). A recent study employed a hybrid DL method, combining a convolutional neural network (CNN) to extract features from significant antecedent inputs of predictor variables and a long short-term memory (LSTM) network to process this information and generate predictions of solar *UVI* (Ahmed et al., 2022). In another study, the efficacy of feature selection (FS) has been highlighted in Alresheedi and Al-Hagery (2020) to effectively handle the challenges related to the curse of dimensionality. Some recent studies have reported the superiority of a wrapper-based recursive feature elimination with cross-validation (RFECV) approach to select an optimal subset from the feature space (Awad and Fraihat, 2023). In principle, RFECV embedded with a tree-based estimator is capable of capturing the non-linearity within the predictor variables and improve generalization performance. Principal component analysis (PCA) is another eminent method proposed by Lan et al. (2019), which efficiently reduces the dimensionality of the input feature space to minimize computational complexity. Yet, none of the previous studies have explored the PCA technique and RFECV FS approach in selecting pertinent climatic variables to optimize the performance of solar *UV-B* radiation forecasting. In addition to effective FS, leveraging a hyperparameter optimization approach further contributes towards achieving an optimal model. Embracing this notion, a prominent Optuna algorithm based on Bayesian optimization is often proposed by researchers as one of the best approaches for exploring optimal hyperparameter configurations (Prasad et al., 2022). Thus, the aforementioned techniques are well-suited for enhancing the accuracy of forecasts for the solar terrestrial *UV-B* waveband.

In the present study, the authors extend on earlier work (Prasad et al., 2023, 2022, 2024), that integrated satellite-derived parameters, sky image-based cloud chromatic properties and the Solar Zenith Angle (SZA) with hybridized DL models to forecast short-term hourly and sub-hourly solar *UVI* and *UV-A*. Among one of these earlier studies, we integrated a deep neural network (DNN) model with explainable AI (*xAI*) tools such as Local Interpretable Model-Agnostic Explanations (LIME) (Ribeiro et al., 2016) and SHapley Additive exPlanations (SHAP) (Lundberg et al., 2020) to efficiently explain the contributions of these atmospheric parameters in forecasting solar *UVI* at local and global levels, respectively. It is commonly accepted that the DL architecture is a black-box system, with hidden internal operations that are complex and not easily explainable (Ribeiro et al., 2016). Embedding the *xAI* tools make the outcomes easy to interpret, transparent and trustworthy for end-users. For the present study, we adopted DL interpretable TabNet model built upon the transformer architecture with multi-dimensional attention mechanism (Arik and Pfister, 2021) to generate forecasts of solar *UV-B* and provide interpretations of the predicted outcomes. TabNet has a deep tabular learning architecture that integrates the benefits of DL and has been used in some other forecasting domains (Ma et al., 2023; Borghini and Giannetti, 2021). At present, a significant gap appears to exist in the literature as none of the hybrid DL frameworks like TabNet have been coupled with the *xAI* tools to deliver accurate predictions and explanations of model outcomes in the domain of forecasting short-term solar *UV-B* radiation from readily attainable atmospheric parameters.

This study makes primary contributions to new knowledge in designing an explainable hybrid TabNet model for the first time and demonstrating its predictive and interpretive skills in forecasting the short-term solar *UV-B* radiation for an experimental site based in Toowoomba, Australia (27.60°S, 151.93°E). We present here a hybridized version of the forecasting system constructed by a fusion of powerful RFECV and PCA techniques for dimensionality reduction, efficient Optuna algorithm for hyperparameter optimization and elegant *xAI*-based LIME and SHAP tools for model explainability. The comparisons of LIME and SHAP methods reveal that LIME approach is more efficient in model execution, but it only delivers instance-based, black-box model interpretations (Islam et al., 2022b). In contrast, the SHAP approach more smartly generates the global explanations for the entire decision of the black-box model, but it entails a higher level of computational complexity (Joseph et al., 2022). Considering that LIME and SHAP methods both have their separate merits and minor deficiencies in respect to the interpretability and explainability of AI models, our study leverages both the tools for delivering efficient model-agnostic explanations of the TabNet model. To depict the influence of atmospheric conditions on ground-level *UV-B* radiation, we integrated our hybrid model with satellite-derived meteorological variables (such as aerosol, precipitation and ozone concentration), sky image-derived cloud statistical properties, SZA and partial autocorrelation function (PACF) of the *UV-B* data-series at the most significant lags.

To make our scientific contributions explicit, hereafter, we denote the newly proposed explainable hybrid TabNet model as X-H-TabNet (*i.e.* where X denotes the explainable, H denotes the hybrid and TabNet denotes the TabNet model), which is the objective model in the *UV-B* forecasting framework. The specific contributions and novelty of this paper are summarized as follows:

- This research assesses the impact of potential satellite-derived environmental variables, sky images, and SZA in the study design, specifically for *UV-B* radiation in Queensland, a region known for elevated solar UV exposure risks in Australia.

- A suitable DL TabNet architecture for tabular data is proposed and implemented for a solar *UV-B* radiation forecasting problem at multiple-step horizons, utilizing a hybridized approach as an optimization strategy.
- Compatible dimensionality reduction methods are applied in the initial stage of model optimization. RFECV FS algorithm is used to extract the informative attributes out of the satellite-derived variables, while PCA is employed to transform the sky image-based cloud statistical properties into principal components by preserving their essential features.
- An Optuna optimizer is applied to further enhance the predictive capability of the *UV-B* forecasting system through efficient tuning of the model hyperparameters.
- The predictive performance of the proposed explainable hybrid X-H-TabNet model is rigorously benchmarked against competing ML and DL models.
- Powerful model-agnostic *xAI* tools are applied to interpret the feature interactions of different atmospheric variables on short-term *UV-B* forecasts. Specifically, the LIME tool generates local explanations while SHAP provides global explanations of the predicted outcomes.
- The accurate and explainable predictions generated by the *UV-B* forecasting system can aid end-users to deliver more precise exposure severity information and sun protection recommendations for people and other terrestrial life taking into account the stochastic nature of the atmosphere over short, hourly to sub-hourly time scales.

The state of Queensland is the primary geographical focus of this study because of its high levels of solar *UV-B* radiation and the prevalence of fair skin types at risk of keratinocyte and melanoma skin cancers. The outcome of the study is to develop an intelligent X-H-TabNet model as a viable solar *UV-B* monitoring tool to help mitigate subsequent risk of harmful exposure impacting the public.

The remainder of this paper is presented as follows: Section 2 discusses the theoretical background. Section 3 describes the different approaches implemented in model design. Section 4 provides the results and discussions for the performance evaluation and interpretations of the *UV-B* forecasting system. Finally, Section 5 outlines the concluding remarks of this study. The list of acronyms are provided in Table A.1.

2. Theoretical overview

In this section, we deliver a succinct background of the algorithms applied in constructing the prescribed explainable hybrid TabNet model. For completeness, we outline the theoretical details of the DL TabNet architecture. Thereafter, we describe the LIME and SHAP techniques in delivering model-agnostic explanations for the predicted outcomes at local and global levels, respectively. Apart from the prescribed explainable hybrid TabNet model, we further developed other competing benchmarked models by utilizing DL and ML as the base models, which includes long short-term memory (LSTM) and gated recurrent unit (GRU), and extreme gradient boosting (XGB), support vector regression (SVR), stochastic gradient descent (SGD), kernel ridge regression (KRR) and decision tree (DT) as the base models. The operational mechanisms and explanations of these counterpart models constructed using LSTM (Jayasinghe et al., 2022), GRU (Jia et al., 2021), XGB (Chen et al., 2019), SVR (Luna et al., 2014), SGD (Tao et al., 2023), KRR (Naik et al., 2018) and DT (Li et al., 2021) are elucidated elsewhere, as these techniques are well-known.

2.1. Deep learning TabNet architecture

TabNet is a remarkable predictive model based on DNN, having capabilities to learn from tabular data (Arik and Pfister, 2021). A basic architecture of TabNet model is presented in Fig. 1. Initially, the input dataset is passed to the model with its specific batch size (B) and D-dimensional features $f \in \mathbb{R}^{B*D}$ to each decision step without applying global feature normalization. TabNet encodes data using a sequence of multi-step processes in N_{steps} decision steps, where the ith step utilizes the processed information from the $(i-1)$th step to determine which features to use, and the resulting feature representation is aggregated into the overall decision. Thereafter, the data is directed to a batch normalization layer, followed by a feature transformer that is configured into three layers, particularly a fully connected layer, a batch normalization layer and a gated linear unit (GLU). For instance, a transformer block concatenated into two shared layers and two decision step-dependent layers, with each layer composed with a fully connected, a batch normalization and a GLU (Dauphin et al., 2017) supports robust and parameter-efficient learning. To secure stability, each block is followed by a $\sqrt{0.5}$ normalization, preventing major fluctuations in variance (Gehring et al., 2017).

After the batch normalized features are processed in the feature transformer block, the output information is passed through a split layer into the attentive transformer at ith step. Basically, an attentive transformer is configured into a four layer network, which include a fully connected, a batch normalization, a prior scales and sparsemax. The input information flow through the split layer passes to the fully connected layer, followed by the batch normalization and prior scales layers. In the prior scales layer, the magnitudes of respective feature attributes is aggregated prior to the current decision step. The prior scale term that denotes the magnitudes of a particular feature being used previously (Arik and Pfister, 2021) is given as:

$$P[i] = \prod_{j=1}^{i} (\gamma - M[j]) \tag{1}$$

where γ is a relaxation parameter.

Using the outcomes of the previous step, the attentive transformer determines the mask layer of the current step. In this regard, soft selection of most salient features is achieved by applying a learnable mask, $M[i] \in \mathbb{R}^{B*D}$, to avoid decision steps from learning irrelevant features and enhance parameter efficiency in the model. The attentive transformer uses the processed features from the preceding step $a[i$ - $1]$ to obtain the masks (Martins and Astudillo, 2016), which is given as:

$$M[i] = sparsemax\left(P[i-1] * h_i\left(a[i-1]\right)\right) \tag{2}$$

where *sparsemax* represents the sparsemax layer applied for coefficient normalization, $P[i$ - $1]$ is the prior scales item and $h_i(\bullet)$ is the trainable function representing the fully connected and batch normalization layers.

It is to be noted that coefficient normalization by the sparsemax layer results in sparse FS (Martins and Astudillo, 2016), where:

$$\sum_{j=1}^{D} M[i]_{b,j} = 1 \tag{3}$$

In this regard, the features having $\sum_{j=1}^{D} M[i]_{b,j} = 0$ are excluded to support better learning by the model. The aforementioned process of masking by the attentive transformer is multiplicative, *i.e.*, $M[i]{*}f$.

An entropy-based sparsity regularization (L_{sparse}) is considered to better manage the sparsity of the selected features (Grandvalet and Bengio, 2004), which is given as:

$$L_{sparse} = \sum_{i=1}^{N_{steps}} \sum_{b=1}^{B} \sum_{j=1}^{D} \frac{-M_{b,j}[i] log(M_{b,j} + \epsilon)}{N_{steps} * B} \tag{4}$$

where ϵ is a small number for numerical stability.

Furthermore, a feature transformer is applied to process the filtered feature attributes, followed by a split into two outputs, given as:

$$[d[i], a[i]] = f_i(M[i] * f) \tag{5}$$

where, $d[i] \in \mathbb{R}^{B*N_d}$ is the decision step output and $a[i] \in \mathbb{R}^{B*N_a}$ is the information for the subsequent step for the attentive transformer that comes next.

Apart from robust predictive capability, the TabNet model also offers interpretable applications using the output vector.

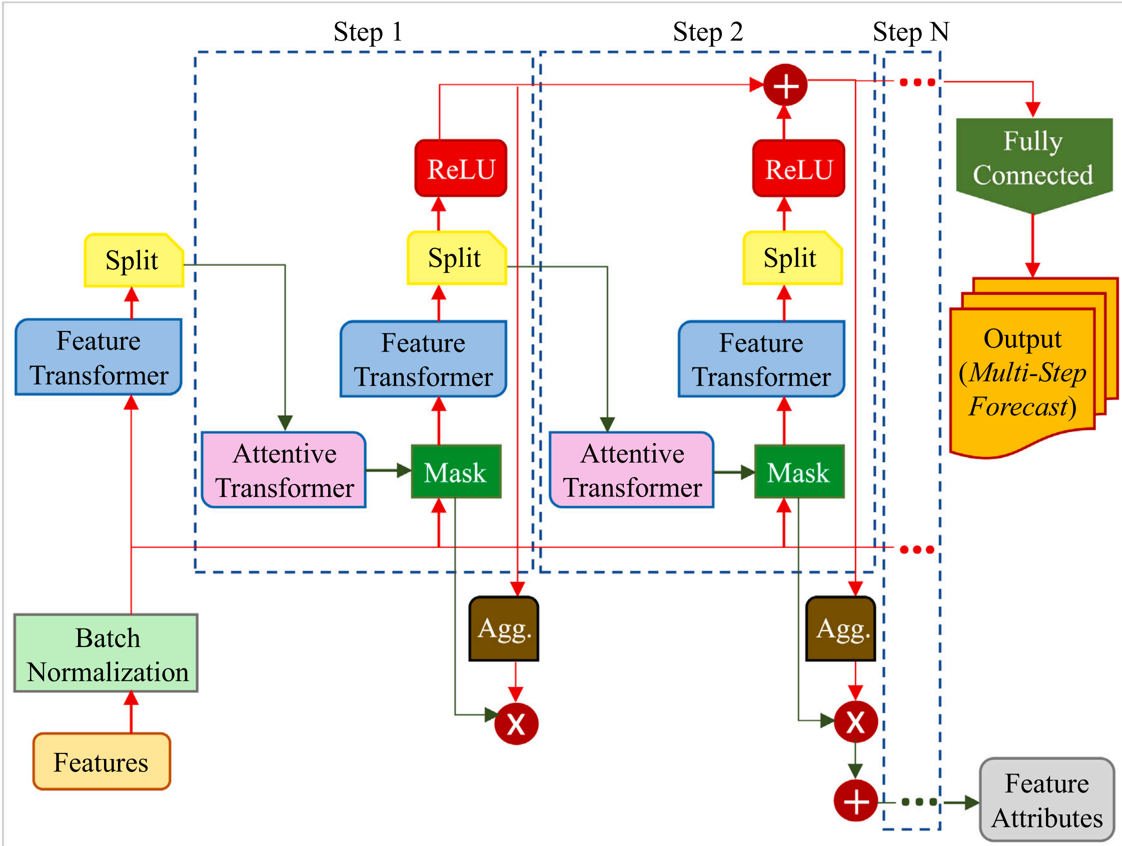

Fig. 1. Schematic view of the standard TabNet architecture.

2.2. Optuna optimizer

In this study, we leveraged Optuna, a flexible and powerful tool for hyperparameter optimization. Optuna streamlines the complex task of fine tuning ML and DL frameworks, to optimize the predictive performance. Featuring a define-by-run API, Optuna platform allows for dynamic construction of the parameter search space, utilizing effective search and pruning techniques for optimal performance (Akiba et al., 2019). For a given search space, Optuna exploits some efficient samplers, including random, grid, Bayesian and genetic calculations to search the best hyperparameter values (Garg and Pundir, 2021). In this regard, Optuna represents each interaction as a study, enhancing the process based on the objective function and trials. Here, a trial refers to each individual evaluation or execution of this function.

The Optuna optimization process unfolds through a number stages (Gao et al., 2021). In the first stage, Optuna determines the optimization direction, range of values, maximum number of iterations and parameter type. The second stage involves the optimization algorithm to step into the loop. Within the loop, individuals from the population are selected uniformly based on the function that defines the range of parameter values. The hopeless individuals in the population are automatically terminated based on trimming conditions using a trimmer. Thereafter, the objective function value for the unpruned individuals is determined. The loop is repeatedly executed and exited after reaching the maximum number of iterations. In the final stage, the optimal solution and function value are extracted as the output.

When compared to other exhausted grid search and random grid search methods, the Optuna algorithm is a next generation hyperparameter optimization tool that can robustly deliver an optimum combination of hyperparameters with relatively lower computation burden (Ekundayo, 2020).

2.3. xAI-inspired local interpretable model-agnostic explanations (LIME)

LIME is a fascinating method for capturing local post-hoc explainability of a black-box predictive model. The captivating aspect of LIME lies in its accessibility and ease of use, as it exploits a surrogate interpretable model to approximate the predictions of a black-box model locally (Ribeiro et al., 2016). While LIME accommodates input datasets in image, text, and tabular formats to facilitate local explanations (Mulwa et al., 2024), our study applies LIME to tabular data format.

To generate an explanation for a given observation, LIME creates replications of the feature data by repeatedly perturbing the input observations. Having the perturbed data, it applies a black-box model to generate predictions and benchmarks this data with respective observed data point. LIME calculates the Euclidean distance between these data points and uses it to reveal the feature variables that are most effective in contributing towards black-box model's predictions.

Overall, LIME generates a set of local explanations that emphasizes on the contribution of each predictor variable to the prediction of a given sample data in a black-box system (Vilone and Longo, 2021). The predictive explanations can be accomplished by creating an explainer, which necessitates LIME to minimize an objective function (Kuzlu et al., 2020), given as:

$$\xi(x) = \underset{g \in G}{\operatorname{argmin}}\, \mathcal{L}(f, g, \pi_x) + \Omega(g), \tag{6}$$

where $\mathcal{L}(f, g, \pi_x)$ measures the level of unfaithfulness in how the explanation model g approximates the predictions of the original black-box model f, π_x is the proximity measure that defines size of the neighborhood around instance x, f represents the explained black-box model, G denotes the set of interpretable models, and $\Omega(g)$ measures the explanation complexity for all $g \in G$. LIME application entails two goals, where the first is to minimize $\Omega(g)$ and the second is to minimize $\mathcal{L}(f, g, \pi_x)$. The first goal is to uphold model simplicity for acquiring quality interpretations. The second major goal is to accomplish an interpretable approximation of the original model at local level. In terms of computational efficiency, LIME is very fast in executing the local explanations.

2.4. xAI-inspired Shapley additive explanations (SHAP)

The basis of SHAP originates from the concept of Shapley values in game theory, aiming to equitably distribute each player's contribution to collectively achieve a particular outcome (Li, 2022). To serve a similar purpose, SHAP algorithm has advanced into a versatile tool that robustly explains the feature interactions of different predictor variables on decisions made by a black-box model in generating predictions (Roth, 1988). For any black-box model, the SHAP value for a feature variable, X_j (Li, 2022; Roth, 1988) is given as:

$$Shapely(X_j) = \sum_{S \subseteq N \setminus \{j\}} \frac{k!\,(p-k-1)!}{p!}\,(f(S \cup \{j\}) - f(S)), \tag{7}$$

where $N \setminus \{j\}$ denotes the set of all possible combinations of predictors except X_j, S defines a feature set in $N \setminus \{j\}$, p represents the total number of predictor variables, $f(S \cup \{j\})$ defines the prediction of a black-box model with both features in S and feature X_j and $f(S)$ defines the prediction of black-box model with features in S. The $Shapely(X_j)$ defines the SHAP value of a predictor variable in terms of the weighted average of the marginal contribution over all possible models with different combinations of predictor variables (Li, 2022).

Showcasing substantial capacity to offer comprehensive black-box model explainability, our study couples the SHAP algorithm with the hybrid TabNet framework to effectively capture the impact of meteorological variables on predicting solar *UV-B* radiation. The efficacy of SHAP has been demonstrated by exploiting a number of skillful explainers (Prasad et al., 2023; Joseph et al., 2024b; Ghimire et al., 2024) and for the purpose of this study, we implement an elegant kernel explainer to generate predictive interpretations of the hybridized TabNet model at global level.

3. Material and methods

This section outlines the methodologies employed in developing and evaluating the proposed explainable hybrid X-H-TabNet model designed for generating solar *UV-B* predictions at multi-step-ahead forecast horizons (*i.e.*, 1-h, 2-h, 3-h, and 4-h). First, the details on the study site and dataset used are described. Secondly, the procedure of extracting the sky image-based cloud statistical properties is detailed. Next, the specific stages used to develop the multiple input, multi-step output X-H-TabNet model are given. Then, the model evaluation criteria used to compare the performance of the proposed and benchmark models are presented. Lastly, details on the *xAI* tools used for model interpretability are outlined.

3.1. Study site and dataset description

To develop and evaluate the X-H-TabNet model, experiments were conducted using data sourced from the Toowoomba campus of the University of Southern Queensland (UniSQ) covering the period between July 1, 2002, and February 29, 2004, resulting in 4826 data points. The study site, positioned at a latitude of 27.60°S and longitude of 151.93°E, is situated in Queensland, often hailed as the 'Sunshine State' (Salcedo-Sanz et al., 2018). With its subtropical climate characterized by warm summers, this region experiences a high frequency of sunny periods throughout the year, averaging around 8.2 h of sunshine per day (Ghimire et al., 2019). Additionally, Queensland's proximity to the equator means that the sun reaches a high elevation for a significant portion of the year, resulting in elevated levels of both visible and *UV* radiation. Previous studies conducted in the region have also investigated short-term effects on the *UV-A* (Prasad et al., 2024) and *UVI* (Prasad et al., 2023), further highlighting the significance of solar radiation in this area.

The considerable exposure to sunlight in this area, accompanied by high levels of *UV-B* radiation, presents notable public health concerns (Dexter et al., 2020). *UV-B* radiation, a component of the sun's ultraviolet light spectrum known for its penetrating energy, can lead to skin damage when exposed for extended periods without protection (Chang et al., 2010). This exposure heightens the risk of various skin cancers, including melanoma, basal cell carcinoma, and squamous cell carcinoma, as evidenced by epidemiological studies (Venugopal et al., 2023; Davis et al., 2021). Queensland, due to its substantial *UV-B* radiation exposure, reports some of the highest skin cancer rates globally (Dexter et al., 2020). Consequently, the state's healthcare system prioritizes addressing this burden, emphasizing the implementation of effective public health strategies to mitigate associated risks.

To acquire the time-series solar *UV-B* dataset for the case study site, a Model 501 Broadband *UV-B* Biometer (Solar Light Company, PA USA) was utilized. This instrument is designed to measure erythemally-weighted broadband *UV-B* solar radiation. Data output from this instrument and others that make up the UniSQ atmospherics research site have recently been made available for public access (mdVine, 2024). The 501 Biometer sensor is located on a rooftop site at the University of Southern Queensland, Toowoomba campus. The instrument dataset consisted of *UV-B* radiation weighted to the human action spectrum for erythema (Commission Internationale de l'Eclairage, 1998). Data set exposures were recorded in units of J cm^{-2} within 5 min intervals. For our *UV-B* forecasting framework, these measurements were converted to the average erythema effective solar *UV* irradiance in mW m^{-2} over 1-h intervals. This conversion and aggregation ensured that the data aligned with our preferred unit and time intervals, facilitating a standardized evaluation of the weighted *UV-B* radiation levels over time. Fig. 2 shows the hourly solar *UV-B* irradiance time-series acquired at the Toowoomba research site. Additionally, the statistical information of the *UV-B* time-series retrieved as the target variable is furnished in Table 1.

The *UV-B* radiation measurements in this dataset exhibit interesting statistical characteristics. With a skewness of 0.7, the distribution shows a moderate rightward skew, indicating that there are more data points on the lower end of the *UV-B* spectrum. This skewness is further complemented by a kurtosis of −0.14, signifying a flatter peak and thinner tails compared to a normal distribution. The mean *UV-B* radiation value of 142.14 mW m^{-2} suggests that, on average, the radiation levels are relatively high, approximating a UVI of 6 over the entire data series.

Furthermore, for model inputs, we integrated data from multiple sources to enhance the accuracy of our predictive models. The satellite-derived predictors used in this study were accessed from the National Aeronautics and Space Administration (NASA) publicly accessible Goddard Online Interactive Visualization and Analysis Infrastructure (GIOVANNI) geoscience data repository available at https://giovanni.gsfc.nasa.gov/giovanni/. From this comprehensive data repository, we chose to leverage the satellite-derived products obtained from the Modern-Era Retrospective Analysis for Research and Applications (MERRA-2) (Berrick et al., 2008). The MERRA-2 data was specifically utilized due to its extensive coverage and reliability in providing accurate and high-quality information regarding atmospheric parameters such as total column ozone (TCO), total aerosol extinction AOT (TAE), total aerosol angstrom parameter (TAAP), total precipitable water vapor (TPWV), and dust extinction AOT (DS) (Table 2). These indices were extracted at a spatial resolution of 0.5° × 0.625°. Another rationale for opting for MERRA-2 datasets was their matching temporal resolution with the *UV-B* radiation data obtained from the Model 501 Broadband *UV-B* Biometer and the sky images captured by the Total Sky Imager. Although MERRA-2 data has coarse spatial resolution, there are methods of extracting finer specific information about smaller and more localized regions by selecting minute gridded area enclosed by four end points of a bounding box. The selected points forming this

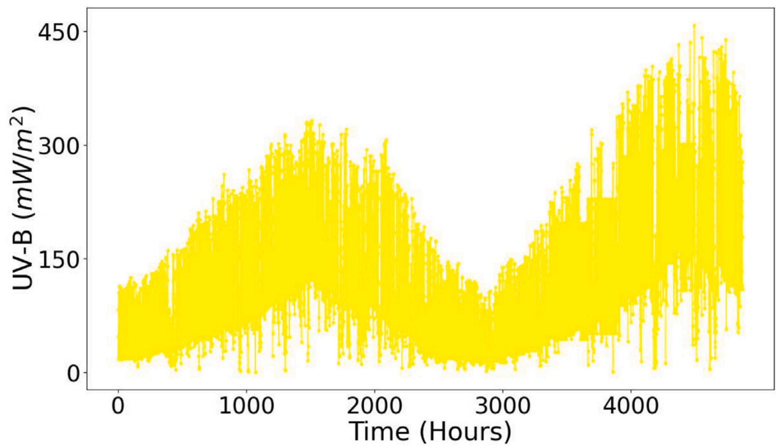

Fig. 2. Hourly solar *UV-B* radiation (mW m^{-2}) time-series for the Toowoomba study site in Queensland where the proposed explainable hybrid TabNet model (*i.e.*, X-H-TabNet) was implemented.

Table 1
(a) Geographical description of the experimental site, (b) Descriptive statistics of erythema weighted ultraviolet B radiation (*UV-B*; mW m^{-2}). (Note: The hourly *UV-B* data are recorded from 01-07-2002 to 29-02-2004.)

(a) Study site, State		Geographical location					
		Latitude (°S)		Longitude (°E)			Elevation (m)
Toowoomba, QLD		27.60		151.95			691
(b) Objective variable	Mean	St. Dev.	Median	Max.	Min.	Skewness	Kurtosis
UV-B	142.14	91.50	123.34	457.98	0.67	0.70	−0.14

Table 2
Descriptions of the satellite-derived and ground-based predictor variables utilized in constructing the proposed explainable hybrid X-H-TabNet model.

Name of attribute	Acronym	Source	Units	Model/Instrument	Spatial resolution
Total column ozone	TCO	MERRA-2	Dobsons	M2T1NXSLV v5.12.4	0.5° × 0.625°
Total aerosol extinction AOT	TAE	MERRA-2	–	M2T1NXAER v5.12.4	0.5° × 0.625°
Total aerosol angstrom parameter	TAAP	MERRA-2	–	M2T1NXAER v5.12.4	0.5° × 0.625°
Total precipitable water vapor	TPWV	MERRA-2	kg m^{-2}	M2T1NXSLV v5.12.4	0.5° × 0.625°
Dust scattering AOT	DE	MERRA-2	–	M2T1NXADG v5.12.4	0.5° × 0.625°
Solar zenith angle	SZA	Model	°	Pro6UV	–

bounding box have very slight differences in longitudes and latitudes. For instance, our study selected a very small gridded region enclosed by the points 151.9292°E, 27.6055°S, 151.9312°E, and 27.6035°S. Here, the datasets of each predictor variable were area-averages of the small selected region at finer spatial resolutions.

Additionally, the SZA attribute recorded by a deterministic Pro6UV model (Deo et al., 2017a) was used as an input (Table 2). The SZA is a valuable predictor of *UV-B* radiation as it measures the angle of the sun relative to a specific location, which directly influences the intensity of UV radiation reaching the Earth's surface (Adam and Ahmed, 2016). A lower SZA angle, corresponding to the compliment of the angular solar elevation, results in a more direct overhead position of the sun, leading to higher *UV-B* radiation levels. We also employed cloud statistical properties as feature attributes, which were extracted from time-dependent whole sky images recorded at the Toowoomba campus university research site (Sabburg and Long, 2004). All sky images were captured at a spatial resolution of 480 × 320 pixels using a Total Sky Imager - TSI440 (TSI) manufactured by Yankee Environmental Systems Inc (in USA). These images were stored in the TSI repository and more information regarding sky image segmentation is given in the following sub-section.

3.2. Extraction of sky image-based cloud statistical properties

Cloud statistical properties have proven to be fundamental predictors in forecasting solar *UV-B* radiation as they significantly influence the level of *UV-B* radiation that reaches the Earth's surface (Ghoneim et al., 2013; Furlan et al., 2012). Clouds can both attenuate and reflect *UV-B* radiation, thereby affecting its intensity and variability. Hence, cloud statistical properties were extracted and utilized as salient inputs to improve the performance of the proposed X-H-TabNet architecture.

To ensure the retrieval of high-quality cloud data, all cloud statistical properties were segmented from the sky images stored in the TSI repository. The TSI repository has a collection of different file types, which include colored sky images in JPEG format, text files containing all relevant metadata related to the images (e.g., sun position, SZA, and cloud fraction), and TSI segmented images in PNG format (Morris, 2005). The segmented images differentiate between different parts of the sky, identifying areas that contain clouds and areas that do not (*i.e.*, clear blue sky). This helped in analyzing cloud coverage and patterns at the Toowoomba measurement site. These segmented images and the cloud fraction information from the text files were used to validate the sky images segmented in this study for the extraction of cloud statistics. This was done by comparing the blue sky and cloud cover components of the TSI segmented PNG image and the segmented image in this present work.

To extract the chromatic properties of clouds, we utilized a highly efficient, self-adaptive sky image segmentation algorithm, which has been tested in our earlier work (Prasad et al., 2022, 2024). This automated algorithm was scripted using the Python programming language (version 3.7.9). In the initialization stage, the algorithm screened all

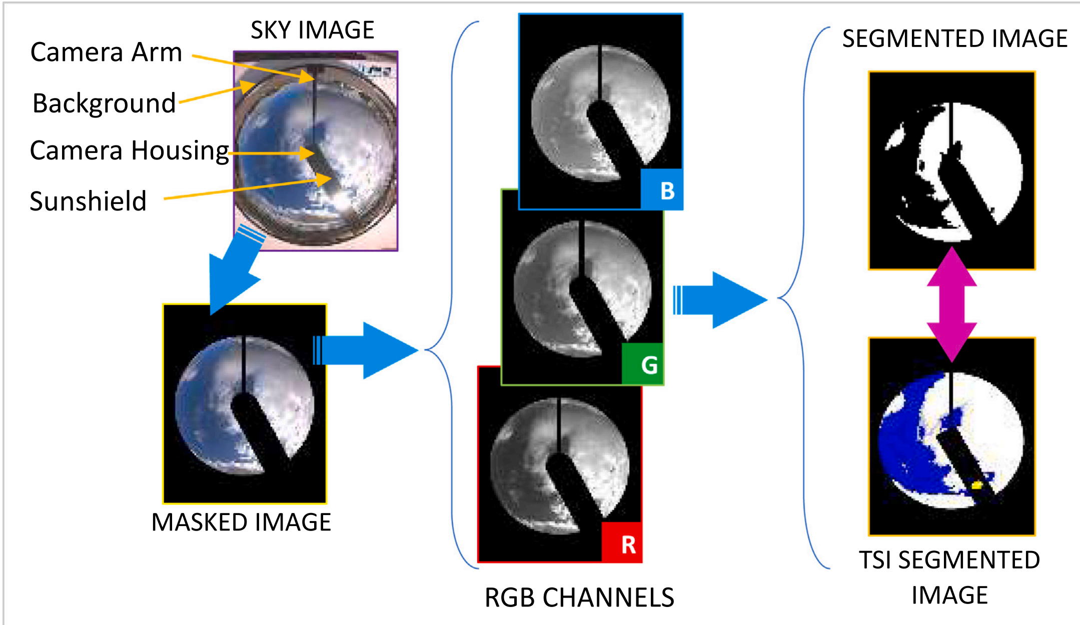

Fig. 3. Process of segmenting whole sky images from the TSI440 repository using the prescribed automated Python tool. The process entails masking of sky image, splitting it into RGB channels, segmenting the image through thresholding and comparing the result with TSI segmented PNG image.

the 10-min sky images in JPEG format and its corresponding meta data from the TSI repository. To ensure best data quality, robust Python libraries, including "linecache", "glob", "os", and "cv2" were employed to read, locate, and report any missing, incomplete, or corrupt images. For valid and uncorrupted sky images, the background, camera housing, camera arm, and sunshield captured were masked using the "numpy" Python-based library. As depicted in Fig. 3, all masked sky images were respectively split into red (R), green (G), and blue (B) channels using the technique devised in Igoe et al. (2019).

Furthermore, the red to blue ratio (RBR) of the R and B channel pixel values were computed and scaled between 0–255 (Igoe et al., 2019). These scaled pixels were binarized and segmented into black and white using a user-defined threshold (T) calculated as follows:

$$T = \frac{255}{RBR_{max}} \times TF \tag{8}$$

where RBR_{max} is the maximum threshold value and TF is a threshold factor with a value of 0.56 (Prasad et al., 2022; Igoe et al., 2019).

The cloud statistical properties of the sky image were extracted by applying a mask to the binarized pixels representing both blue sky and cloud cover onto the blue and red channel pixels. This method ensured that only the relevant areas were considered for analysis. As described in Table 3, a total of seventeen cloud statistical properties were efficiently extracted for all real-time sky images using an automated "for loop", and their correlations with the *UV-B* irradiance measured over the July 2002 to February 2004 measurement period were examined. An extensive retrieval of cloud properties helped provide a comprehensive understanding of cloud patterns and characteristics.

Moreover, the segmentation of the sky image using our algorithm closely matched the segmented PNG image derived automatically by the TSI440 software. Our image segmentation algorithm, derived from the work of Prasad et al. (2022), exhibited a minute ≈1.84% cloud percentage difference between the segmented image and the TSI PNG image. Additionally, it demonstrates a robust correlation of ≈0.991 between the calculated and original TSI440 cloud fraction data, making the extracted attributes good predictors of *UV-B*.

3.3. Input data preprocessing

To obtain reliable *UV-B* forecasting results, a comprehensive dataset was structured, incorporating satellite and ground-based variables (Table 2) as well as statistical properties derived from cloud images (Table 3). These diverse data sources were meticulously prepared to serve as inputs for the proposed and benchmark forecasting models. Firstly, the input and target data were screened for missing data points and extreme outliers across both the training and testing partitions. Missing data can lead to incomplete patterns, making it difficult for the model to learn and generalize effectively (Lyngdoh et al., 2022). On the other hand, outliers can skew the model's understanding of the data distribution, leading to inaccurate predictions and reduced model performance (Li et al., 2015). In our study, we had very few instances where the input datasets were missing. Nevertheless, the sporadic missing data and outliers were imputed using the monthly median imputation approach of corresponding variables (Ochieng'Odhiambo, 2020) to overcome the aforementioned issues. This ensured that the predictive model could make reliable and trustworthy predictions based on clean and representative data. Once the complete datasets were obtained through median imputation and data replacement methods, the stationarity of these datasets was evaluated using the augmented Dickey–Fuller (ADF) Test (Dickey and Fuller, 1979). The ADF test is a statistical test used to determine whether a time series is stationary, meaning its statistical properties like mean and variance do not change over time. The test results confirmed that all the input datasets were stationary and suitable for modeling.

Furthermore, the cross-correlation coefficient (r_{cross}) was evaluated for all predictor variables listed in Tables 2 and 3 to identify the most significant time-lagged relationships for modeling *UV-B*. This process obtained r_{cross} values to determine how well these variables correlated with the *UV-B* target attribute at different time lags. A 95% confidence band was used as a reference, where the lagged components of any variable within this boundary were considered insignificant. By assessing these correlations, we could identify the time delays at which each variable had the strongest relationship with *UV-B* levels. After evaluating r_{cross} for each feature with *UV-B*, the most significant historically preceding values of the predictor variables were selected as inputs to construct the proposed multi-step-ahead hourly *UV-B* forecasting system. Additionally, for more robust outcomes, a PACF statistical assessment was conducted to obtain another set of predictor variables. PACF was employed to identify the optimal lags of antecedent *UV-B* levels, with the first six lags determined to be highly correlated

Table 3
Descriptions of the satellite-derived and ground-based predictor variables utilized in constructing the proposed explainable hybrid X-H-TabNet model.

Cloud statistical properties	Acronym	Description	r_{cross} with *UV-B*
Ratio of captured sky in red and blue channels	RSRB	Ratio of average pixel values in red and blue channels captured with blue sky	0.312
Difference of captured sky in red and blue channels	DSRB	Difference of average pixel values in red and blue channels captured with blue sky	−0.205
Average of captured cloud in red channel	ACR	Average of pixel values in red channel captured with cloud cover	−0.201
Average of captured cloud in blue channel	ACB	Average of pixel values in blue channel captured with cloud cover	−0.195
Standard deviation of captured cloud in blue channel	SCB	Standard deviation of pixel values in blue channel captured with cloud cover	0.189
Opaque cloud	OC	Proportion of thick cloud cover in the blue sky	−0.118
Difference of captured cloud in red and blue channels	DCRB	Difference of average pixel values in red and blue channels captured with cloud cover	−0.107
Average of captured sky in blue channel	ASB	Average of pixel values in blue channel captured with blue sky	−0.101
Cloud fraction	CF	Fraction of the number of cloud captured pixels and total number of unmasked pixels	−0.092
Standard deviation of captured sky in blue channel	SSB	Standard deviation of pixel values in blue channel captured with blue sky	−0.060
Standard deviation of captured sky in red channel	SSR	Standard deviation of pixel values in red channel captured with blue sky	−0.048
Normalized ratio of captured cloud in red and blue channels	RCNRB	Normalized ratio of average pixel values in red and blue channels captured with cloud cover	−0.042
Standard deviation of captured cloud in red channel	SCR	Standard deviation of pixel values in red channel captured with cloud cover	0.035
Normalized ratio of captured sky in red and blue channels	RSNRB	Normalized ratio of average pixel values in red and blue channels captured with blue sky	0.034
Red and blue channel-based cloud ratio	RCRB	Red and blue channel-based mean pixel value ratio that represents cloud cover	−0.031
Thin cloud	TC	Proportion of thin cloud cover in the sky	−0.023
Average of captured sky in red channel	ASR	Average of pixel values in red channel captured with blue sky	0.014

predictors of *UV-B*. These lags are denoted as UVB(t-1), UVB(t-2), UVB(t-3), UVB(t-4), UVB(t-5) and UVB(t-6), where t represents the time component. By incorporating these specific lags, the forecasting model can effectively utilize historical *UV-B* irradiance data to enhance its predictive accuracy for future *UV-B* levels.

3.4. Feature selection

A recursive feature elimination with cross-validation (RFECV) method was employed to identify the most significant satellite-derived and ground-based predictor variables among the six furnished in Table 2, ensuring that only the most impactful predictors were included in the model. Additionally, Principal Component Analysis (PCA) was applied to the 17 cloud statistical properties (Table 3), reducing their dimensionality while retaining the most informative components. The combination of RFECV and PCA allowed for an efficient and effective selection of features, enhancing the model's predictive performance by focusing on the most relevant data.

3.4.1. Recursive Feature Elimination with Cross-Validation (RFECV)

RFECV is an effective wrapper-based FS technique, particularly useful when aiming to enhance model simplicity and performance. Practically, this FS framework employs a ML algorithm to select the optimal feature subsets from the entire feature space FS (Freytes et al., 2023). To enhance robustness, RFECV integrates recursive feature elimination with cross-validation to determine the optimal set of features that maximize the performance of the predictive model (Awad and Fraihat, 2023). RFECV dynamically determines the optimal number of features by iteratively removing them and selecting the best subset based on model performance, without needing a predefined number of features (Shi et al., 2024). Some previous studies have applied RFECV, having the base ML algorithm as DT and RF to classify Alzheimer's disease (Freytes et al., 2023) and to detect intrusions (Merlin and Ravi, 2023). For the purpose of this study, we applied RFECV by incorporating RF model as the base ML algorithm with 5-fold cross-validation. Through integration of RFECV, the complex non-linear interactions between *UV-B* radiation and predictors are more accurately captured. The RFECV algorithm assigns importance scores to features using an iterative process and selects the optimal number of features, as highlighted in Fig. 4 for 1-hourly, 2-hourly, 3-hourly, and 4-hourly forecast horizons. For all forecast horizons, it is observed that RFECV for number of features corresponding to 1 = SZA, 2 = SZA + TAAP, 3 = SZA + TAAP + TAE, 4 = SZA + TAAP + TAE + DE, 5 = SZA + TAAP + TAE + DE + TCO, and 6 = SZA + TAAP + TAE + DE + TCO + TPWV. To determine the number of most informative features, the red dashed vertical line marking the threshold for optimal feature selection serves as a reference. In accordance with this vertical line, RFECV execution iteratively selected all the six predictor variables as pertinent inputs towards model development for each forecast horizon.

3.4.2. Principal Component Analysis (PCA)

PCA (Malhi and Gao, 2004) is an effective dimensionality reduction technique, which aims to transform a dataset with multiple correlated variables into a smaller set of uncorrelated variables called principal components. These principal components capture the maximum variance in the data while minimizing information loss. In this study, we analyze 17 cloud statistical property attributes derived from segmented cloud images using the PCA multivariate analysis technique. Let us suppose that $\mathbf{X}$ is the predictor variable matrix of dimension $m \times n$, where m indicates the total number of cloud statistical attributes (*i.e.*, 17) and n is the total number of data points in the dataset. Based on this, the individual predictors f_{1-17} from the matrix $\mathbf{X}$ were vectorized into $\widetilde{\upsilon_j} = \mathbb{R}^{mn\times 1}$ where $j = 1, 2, \ldots, 17$. Then, the individual feature vectors $\widetilde{\upsilon_j}$ were stacked to form the matrix $\hat{\mathbf{X}} \in \mathbb{R}^{mn\times 17}$ as follows:

$$\hat{\mathbf{X}} = \left[\widetilde{\upsilon_1},\ \widetilde{\upsilon_2},\ \widetilde{\upsilon_3}, \ldots,\ \widetilde{\upsilon_{17}}\right] \tag{9}$$

The PCA was performed on the normalized matrix of $\hat{\mathbf{X}}$ using the corresponding feature vector means $\bar{\upsilon_j}$ and standard deviations σ_{υ_j}. The normalized matrix $\ddot{\mathbf{X}}$ was computed as:

$$\ddot{\mathbf{X}} = \left[\frac{\widetilde{\upsilon_1} - \bar{\upsilon_1}}{\sigma_{\upsilon_1}}, \frac{\widetilde{\upsilon_2} - \bar{\upsilon_2}}{\sigma_{\upsilon_2}}, \frac{\widetilde{\upsilon_3} - \bar{\upsilon_3}}{\sigma_{\upsilon_3}}, \ldots, \frac{\widetilde{\upsilon_{17}} - \bar{\upsilon_{17}}}{\sigma_{\upsilon_{17}}}\right] \tag{10}$$

The Eigenvalues and Eigenvectors were computed from the normalized covariance matrix calculated using Eq. (10). These Eigenvalues represent the variance explained by each Eigenvector, with the Eigenvectors themselves forming the principal components (PCs) of the dataset. From this analysis, 6 PCs (denoted as PCA1, PCA2, PCA3, PCA4, PCA5 and PCA6) were carefully selected based on their corresponding Eigenvalues. This selection process ensures that these 6 components collectively capture a substantial amount of variability present in the cloud statistical properties data.

The variance explained rates for the 6 PCs in conducting PCA on the training and testing data series of cloud statistical properties are summarized in Table 4. These explained rates indicate the percentage

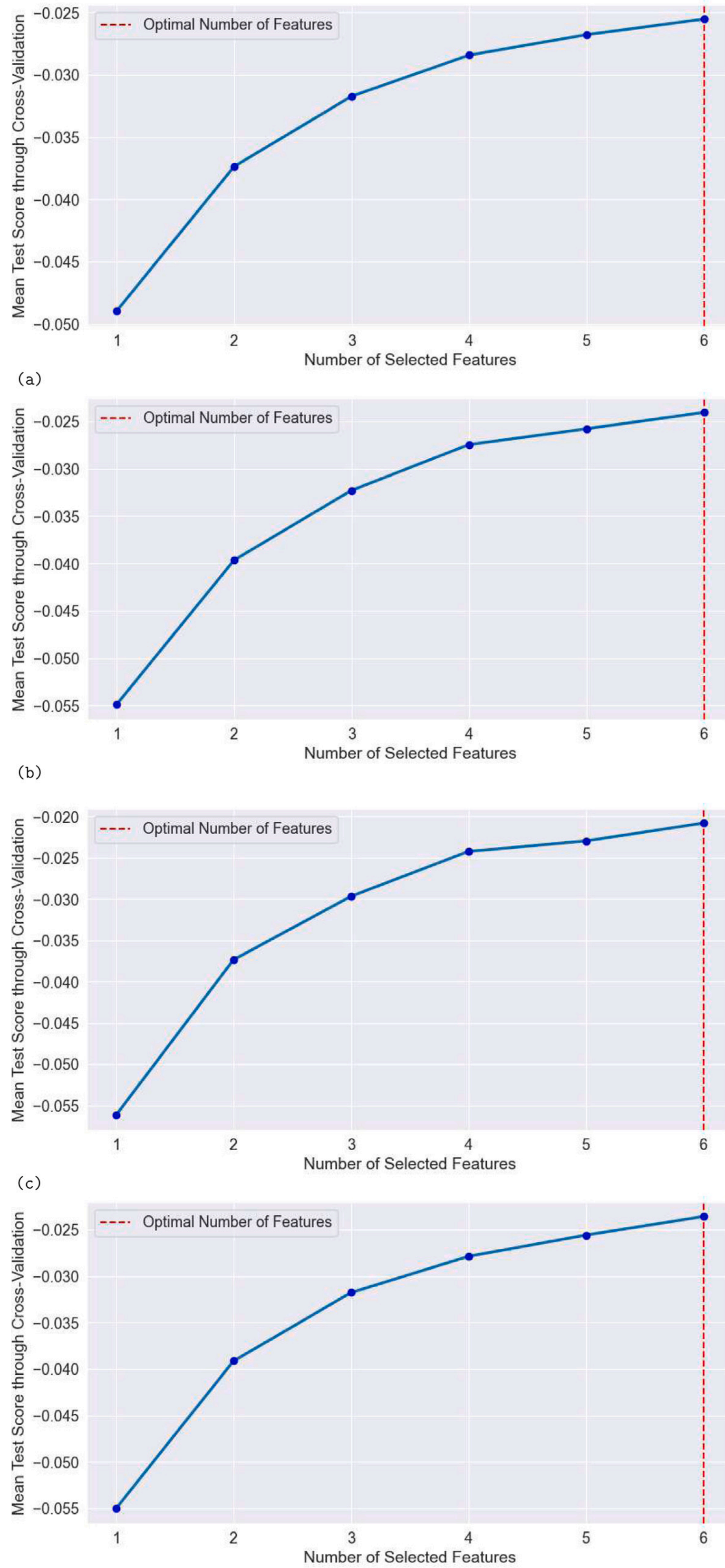

Fig. 4. Selection of pertinent features from a pool of six satellite-derived and ground-based predictor variables using recursive feature elimination with cross-validation (RFECV) method; where the red dashed vertical line marking indicates the threshold for the optimal number of features selected in the design phase of the explainable hybrid TabNet framework.

Table 4
Variance explained rates for the six principal components in conducting the principal component analysis (PCA) for the training and testing data series of the cloud statistical properties.

Dataset	Variance explained rate (%)			
	Hourly horizon	2 hourly horizon	3 hourly horizon	4 hourly horizon
Training	99.32	99.32	99.32	99.32
Testing	99.62	99.62	99.62	99.62

of variance in the data that is explained by each PC across different time horizons. The consistently high rates (ranging from around 99.32% to 99.62%) for both training and testing datasets demonstrate that the selected PCs effectively capture the variability present in the cloud statistical properties data. This high level of variance explained suggests that the PCA process successfully summarizes the essential information in the dataset while reducing its dimensionality, contributing to more efficient and accurate modeling and analysis.

3.5. Proposed UV-B multi-step-ahead forecast model development

After the data cleaning and FS stages, the explainable hybrid TabNet model was developed for multi-step-ahead *UV-B* forecasting. The model pipeline, graphically presented in Fig. 5 was built using the Python programming language on the Google Colaboratory platform, leveraging a graphical processing unit (GPU) for enhanced performance. This virtual environment offers a suite of powerful packages, such as Scikit-learn (Pedregosa et al., 2011), Keras (Ketkar and Ketkar, 2017), and TensorFlow (Abadi et al., 2016), renowned for their capabilities in executing state-of-the-art ML and DL algorithms.

Before inputting the target and predictor data into the model, the datasets underwent normalization to ensure that each variable had a consistent scale within the range of [0–1]. This normalization procedure, known as min–max normalization (Islam et al., 2022a) was performed using the following computation to obtain the normalized input data X_{NORM}:

$$X_{NORM} = \frac{X_{ACT} - X_{MIN}}{X_{MAX} - X_{MIN}} \tag{11}$$

where X_{ACT} is the actual input data, and X_{MIN} and X_{MAX} include the minimum and maximum values of the input data, respectively.

To successfully develop a robust *UV-B* simulating model using AI framework, the entire datasets were first partitioned into training, validation and testing. In the absence of a standard approach for dividing data into training and testing sets, this study employed 80% of the datasets for training, and 20% for testing. By applying this splitting ratio to a total of 4826 data points, 3863 points were allocated to the training set, and 963 to the testing set. It is to be noted that a data split ratio similar to that of our study was also employed by Wong et al. (2021) for predicting ground level $PM_{2.5}$. In the present study, we ensured that the training datasets (*i.e.*, 80%) included only observations that precede those in the testing datasets (*i.e.*, 20%). Additionally, the data segregation strategy adopted in this study aligns with existing literature, which emphasizes the importance of partitioning the entire dataset into training and testing subsets before building the model to prevent the leakage of training data into future testing data, thus avoiding testing bias (Deo et al., 2017b). On the same note, our study employed time series cross-validation to enhance the robustness of the model evaluation. We applied 10-fold cross-validation technique by selecting 10% of the training portion for validation (Wong et al., 2021). In the 10-fold cross-validation approach, 90% of the randomly selected data was used for model training, and 10% was designated for testing. This cycle was repeated ten times, allowing each fold to be tested exactly once. By employing 10-fold cross-validation, the performance of the proposed hybrid Tabnet model became more reliable, as it was tested on different train–test splits during the validation phase.

Essentially, the study integrated the 10-fold cross-validation approach with a hyperparameter optimization algorithm to derive fine-tuned hyperparameters for the optimal predictive model. For this purpose, a powerful Optuna optimizer was fused with the objective hybrid TabNet model, as well as other benchmarked models. Optuna is an advanced optimization framework designed to automate the search for optimal hyperparameters (Srinivas and Katarya, 2022). This method facilitated a comprehensive evaluation of TabNet's performance against the comparative counterparts. It helped in identifying the best hyperparameter settings by minimizing overfitting and improving generalizability. The optimal hyperparameters for the proposed TabNet models, tailored for each of the four forecast horizons, are detailed in Table 5. The proposed hybrid TabNet model enhanced through robust FS methods and efficient hyperparameter tuning (*i.e.*, X-H-TabNet) was evaluated and benchmarked against 7 state-of-the-art hybridized models. For ease of distinction, the descriptions and acronyms of these models are provided in Table 6.

3.6. Model evaluation criteria

The use of diverse performance measures is essential for effectively comparing predictive models (Joseph et al., 2023). While a single metric may provide valuable information, it often fails to capture the full complexity and nuances of a model's performance. By utilizing multiple metrics, we can gain diverse perspectives that collectively offer a more comprehensive assessment. This multifaceted approach not only enhances our understanding of a model's strengths and weaknesses but also guides decision-making processes more effectively in terms of model selection, optimization, and deployment strategies (Joseph et al., 2024b). Hence, four powerful statistical metrics, namely Pearson's Correlation Coefficient (r), Mean Absolute Error (*MAE*), Root Mean Squared Error (*RMSE*), and Legate-McCabe Efficiency Index (*LME*) were used for rigorous assessment of the proposed X-H-TabNet model against the benchmark models in forecasting multi-step-ahead *UV-B*. The use of these measures is strongly recommended in solar radiation and UV-based forecasting studies (Qin et al., 2020; Ghimire et al., 2022; Ahmed et al., 2022; Deo et al., 2018). The mathematical expressions of these statistical metrics are given as follows:

Mathematically, these metrics can be represented as:

$$r = \frac{\sum_{i=1}^{N}\left(\text{UV-B}_i^O - \overline{\text{UV-B}}^{\,O}\right)\left(\text{UV-B}_i^F - \overline{\text{UV-B}}^{\,F}\right)}{\sqrt{\sum_{i=1}^{N}\left(\text{UV-B}_i^O - \overline{\text{UV-B}}^{\,O}\right)^2}\sqrt{\sum_{i=1}^{N}\left(\text{UV-B}_i^F - \overline{\text{UV-B}}^{\,F}\right)^2}}, \tag{12}$$

$$MAE = \frac{1}{N}\sum_{i=1}^{N}\left|\text{UV-B}_i^O - \text{UV-B}_i^F\right|, \tag{13}$$

$$RMSE = \sqrt{\frac{1}{N}\sum_{i=1}^{N}(\text{UV-B}_i^O - \text{UV-B}_i^F)^2}, \tag{14}$$

and

$$LME = 1 - \frac{\sum_{i=1}^{N}\left|\text{UV-B}_i^O - \text{UV-B}_i^F\right|}{\sum_{i=1}^{N}\left|\text{UV-B}_i^O - \overline{\text{UV-B}}^{\,O}\right|}, \tag{15}$$

where N is the total number of paired UV Index and predictor data points, UV-B_i^O and UV-B_i^F are observed and forecasted *UV-B* for the i^{th} observation, $\overline{\text{UV-B}}^{\,O}$ and $\overline{\text{UV-B}}^{\,F}$ are average observed and average forecasted *UV-B*. The values of r range between −1 to +1, where the two extremes are ideal values. The error values of *MAE* and *RMSE* range from 0 to ∞, where 0 and ∞ imply a perfect fit and worst fit, respectively. The *LME* can robustly address the predictive limitations and it ranges between 0 to 1, where 1 is an ideal value.

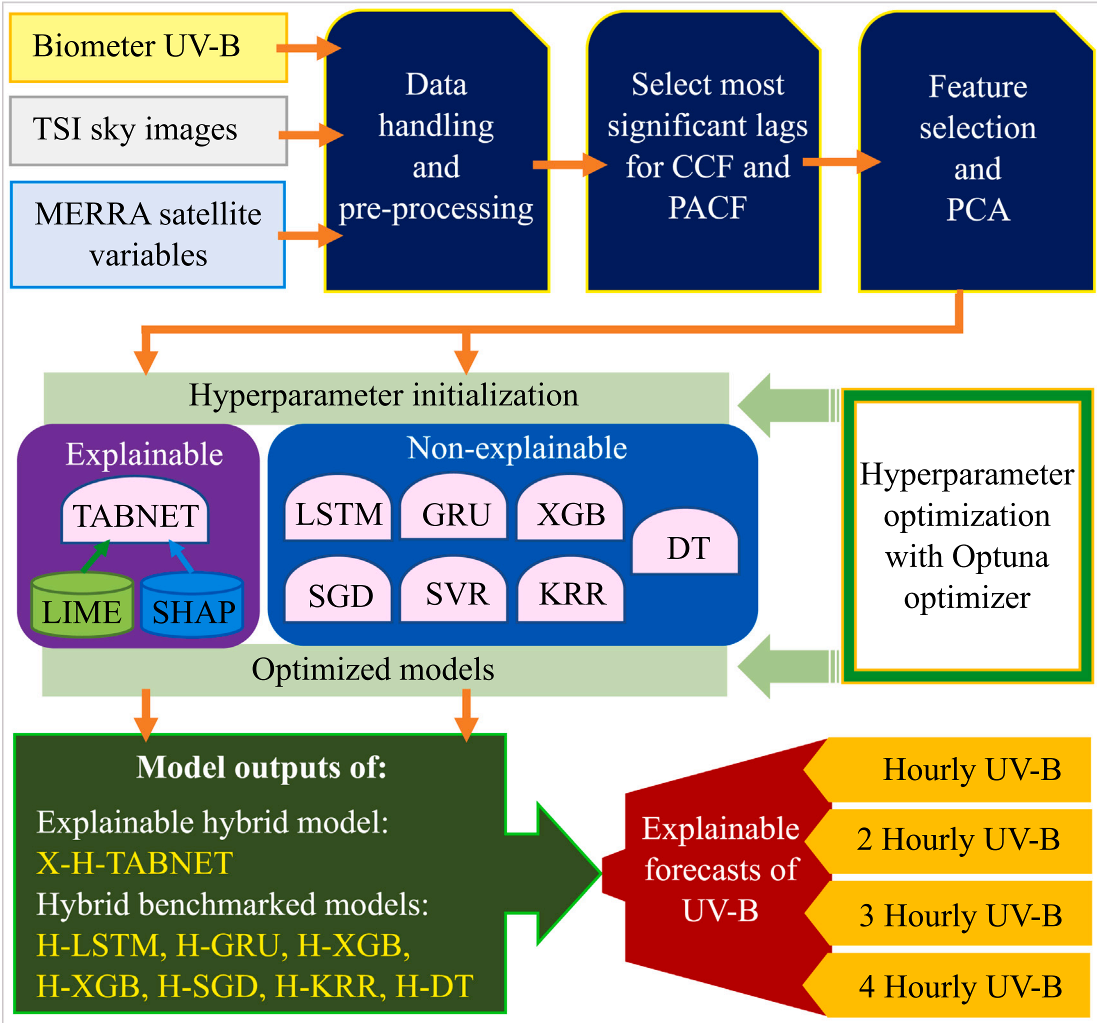

Fig. 5. Flowchart detailing the proposed multiple input, multi-step output model for solar *UV-B* forecasts based on explainable hybrid X-H-TabNet model.

3.7. Model explainability

It is important to note that while model performance is of utmost importance, interpretability plays a significant role as well. Understanding how and why a model makes predictions is essential for gaining insights, ensuring transparency, and building trust in the model's capabilities (Joseph et al., 2022). Hence, *xAI*-based model-agnostic explainers (*i.e.*, LIME and SHAP) were used to provide insights into the predictions generated by the proposed X-H-TabNet architecture designed for *UV-B* forecasting.

First, LIME was employed to achieve local explainability of the predictive outcomes. This involved visualizing the influence of all features on the 50th and 100th instances of the test data for each of the four forecast horizons through bar plots. Following this, the SHAP explainer was utilized for global explainability, showcasing the impact of individual features on the overall model performance using beeswarm and feature dependence plots.

4. Results and discussion

This study introduces the hybrid TabNet model (X-H-TabNet) alongside other hybrid deep learning and machine learning models to forecast multi-step *UV-B* solar radiation. The performance of the proposed hybrid TabNet model is rigorously evaluated against alternative hybrid deep learning and machine learning models using key statistical metrics, including the correlation coefficient (r), root mean square error ($RMSE$), and mean absolute error (MAE), applied to the testing dataset. The X-H-TabNet model demonstrated superior performance in predicting *UV-B* values for an hourly horizon, achieving a high correlation coefficient ($r \approx 0.908$) and relatively low values for both root mean square error ($RMSE \approx 25.944$) and mean absolute error ($MAE \approx 18.04$) (Refer Table 7). For two-hourly, three-hourly, and four-hourly horizons, the model also maintained strong predictive accuracy, with respective r, $RMSE$, and MAE values of $\approx 0.88, \approx 28.203, \approx 17.169; \approx 0.868, \approx 31.302, \approx 20.233$; and $\approx 0.868, \approx 29.533, \approx 19.424$. Among the benchmark models, the hybrid machine learning model XGB (H-XGB) outperformed hybrid deep learning models (H-LSTM and H-GRU) in terms of accuracy. For instance, in the hourly horizon, the H-XGB model achieved an r value of ≈ 0.892, $RMSE$ of ≈ 27.085, and MAE of ≈ 18.659, compared to H-LSTM ($r \approx 0.881$, $RMSE \approx 29.713$, $MAE \approx 22.262$) and H-GRU ($r \approx 0.885$, $RMSE \approx 29.849$, $MAE \approx 22.337$). The outstanding performance of the X-H-TabNet model across all forecast horizons underscores its potential as a robust forecasting approach for *UV-B* predictions, surpassing other benchmark models, including hybrid deep learning models (H-GRU and H-LSTM) and hybrid machine learning models (H-XGB, H-SVR, H-SGD, H-KRR, and H-DT).

Table 5
Optimal architecture of the explainable hybrid X-H-TabNet model and the hybrid benchmarked models developed for multiple time-scale *UV-B* forecasts.

Designed models	Model hyperparameters	Hyperparameter search space	Fine tuned hyperparameters with optuna: Hourly horizon	2 hourly horizon	3 hourly horizon	4 hourly horizon
X-H-TabNet	mask_type	[entmax, sparsemax]	sparsemax	sparsemax	sparsemax	sparsemax
	n_d, n_a	[56, 60, 64], [56, 60, 64]	56, 64	56, 60	56, 60	56, 60
	n_steps, n_shared	[1, 2, 3], [1, 2, 3]	3, 2	3, 2	3, 2	3, 2
	gamma, virtual_batch_size	[1.0, 1.2, 1.4], [10, 20]	1.0, 10	1.0, 10	1.0, 10	1.0, 10
	lambda_sparse	[1×10^{-6} to 1×10^{-3}]	5.3×10^{-4}	7.3×10^{-4}	7.1×10^{-4}	4.5×10^{-4}
	batch_size	[40 to 200, step = 20]	80	80	80	80
	epochs	[40 to 200, step = 20]	260, 300	290, 280	200, 200	200, 200
	patience	[3 to 10, step = 1]	6	6	6	6
	learning_rate, step_size	[2×10^{-2}], [10]	2×10^{-2}, 10			
H-LSTM	units 1	[40 to 150, step = 5]	55	50	55	55
	units 2	[10 to 60, step = 5]	50	50	50	45
	units 3	[5 to 45, step = 5]	45	45	45	45
	batch_size	[60 to 120, step = 10]	70	70	75	75
	epochs	[100, 150, 200, 250]	250	250	250	250
	optimizer, learning_rate	[Adam], [0.001]	Adam, 0.001			
	dropout, patience, activation	[0.1], [20], [ReLU]	0.1, 20, ReLU			
	beta_1, beta_2, epsilon	[0.9], [0.999], [1×10^{-10}]	0.9, 0.999, 1×10^{-10}			
H-GRU	units 1	[40 to 150, step = 5]	55	50	55	50
	units 2	[10 to 60, step = 5]	50	45	50	40
	units 3	[5 to 45, step = 5]	50	40	45	40
	batch_size	[60 to 120, step = 10]	75	75	70	70
	epochs	[100, 150, 200, 250]	250	250	250	250
	optimizer, learning_rate	[Adam], [0.001]	Adam, 0.001			
	dropout, patience, activation	[0.1], [20], [ReLU]	0.1, 20, ReLU			
	beta_1, beta_2, epsilon	[0.9], [0.999], [1×10^{-10}]	0.9, 0.999, 1×10^{-10}			
H-XGB	n_estimators	[100, 150, 200]	100	100	150	100
	max_depth	[5, 10]	5	5	5	5
	eta	[0.1, 0.2, 0.3, 0.4, 0.5]	0.1	0.1	0.1	0.3
	gamma	[0.2, 0.4]	0.2	0.4	0.4	0.4
	min_child_weight	[1, 3, 5]	5	5	3	1
H-SVR	kernal	[poly, rbf, sigmoid]	rbf	rbf	rbf	rbf
	gamma	[scale, auto]	scale	scale	scale	scale
	epsilon	[0.1, 5.0, step = 0.1]	1.0	1.7	0.6	0.9
	degree	[2, 3, 4, 5, 6]	6	6	5	6
H-SGD	eta0	[0.01, 0.02, 0.03]	0.03	0.03	0.02	0.03
	power_t	[0.25, 0.35]	0.25	0.25	0.25	0.25
	max_iter	[500, 1000, 1500]	1000	1500	1500	1000
	tol	[0.001, 0.002, 0.003]	0.002	0.001	0.001	0.001
H-KRR	alpha	[1, 2, 3]	3	1	1	3
	kernel	[linear, polynomial]	linear	linear	polynomial	linear
	degree	[2, 3, 4]	3	2	3	3
	coef0	[1, 2, 3]	1	1	3	1
H-DT	min_samples_split	[2, 4, 6, 8]	6	4	6	6
	max_depth	[5, 10, 15]	5	10	10	10
	min_samples_leaf	[2, 6, 10]	10	2	10	6
	max_features	[log2, auto, sqrt]	auto	auto	log2	sqrt

Table 6
Descriptions and respective designations of the multiple input multi-step output hybridized deep learning and machine learning models constructed to generate short-term *UV-B* forecasts.

Description of model		Designation
Prescribed *xAI* model:	Explainable hybrid TabNet	X-H-TabNet
Counterpart models:	Hybrid LSTM	H-LSTM
	Hybrid GRU	H-GRU
	Hybrid XGB	H-XGB
	Hybrid SVR	H-SVR
	Hybrid SGD	H-SGD
	Hybrid KRR	H-KRR
	Hybrid DT	H-DT

Fig. 6 illustrates the Legates and McCabe's index (LME) for the forecasted and actual *UV-B* values generated by the X-H-TabNet model, compared to the H-LSTM, H-GRU, H-XGB, H-SVR, H-SGD, H-KRR, and H-DT models. This index is particularly valuable as it considers the absolute differences between forecasted and actual data, as well as the variability inherent in the actual data, offering a more comprehensive evaluation of model performance. The robustness of LME to outliers and its ability to handle diverse data distributions further enhance its utility in model assessment. The results depicted in Fig. 6 demonstrate that the X-H-TabNet model consistently outperforms all the other comparative hybrid deep learning and machine learning models across all forecast horizons. This superior performance is evident when considering higher-order metrics like LME, in addition to traditional metrics such as r, $RMSE$, and MAE. The X-H-TabNet model's advanced predictive capabilities enable it to provide highly accurate forecasts of *UV-B* radiation, making it a promising candidate for implementation in *UV-B* prediction tasks. The consistent excellence of the X-H-TabNet model, as shown by the LME, underscores its effectiveness and reliability in capturing the intricate patterns and dependencies present in *UV-B* data.

Furthermore, Fig. 7 presents a scatterplot for the hourly forecast horizon, illustrating the correlative relationship between the forecasted and observed *UV-B* values through a linear equation, $y = mx + c$, accompanied by the coefficient of determination, R^2. In this context,

Table 7
Testing phase performance of the proposed X-H-TabNet model alongside the benchmarked counterparts to forecast multi-step ahead *UV-B* radiation. The statistical metrics of r, MAE, and RMSE represent correlation coefficient, mean absolute error, and root mean square error.

Predictive	Hourly horizon			2 hourly horizon			3 hourly horizon			4 hourly horizon		
model	*r*	*MAE*	*RMSE*	*r*	*MAE*	*RMSE*	*r*	*MAE*	*RMSE*	*r*	*MAE*	*RMSE*
X-H-TabNet	0.908	25.944	18.040	0.880	28.203	17.169	0.868	31.302	20.223	0.868	29.531	19.424
H-LSTM	0.881	29.713	22.262	0.864	29.960	20.146	0.862	31.259	22.358	0.858	32.755	23.348
H-GRU	0.885	29.849	22.337	0.860	30.999	21.004	0.866	30.608	21.143	0.860	30.380	19.792
H-XGB	0.892	27.085	18.659	0.875	29.133	18.755	0.867	30.444	20.081	0.845	32.978	22.537
H-SVR	0.875	31.013	21.981	0.861	30.730	20.440	0.855	30.877	19.749	0.852	31.126	20.263
H-SGD	0.871	29.610	20.821	0.858	30.636	20.275	0.853	31.014	20.023	0.852	31.275	20.087
H-KRR	0.876	28.814	20.391	0.862	30.290	20.222	0.854	30.867	20.217	0.853	31.260	20.140
H-DT	0.847	32.543	21.537	0.837	32.823	21.752	0.782	39.663	26.840	0.803	35.739	25.537

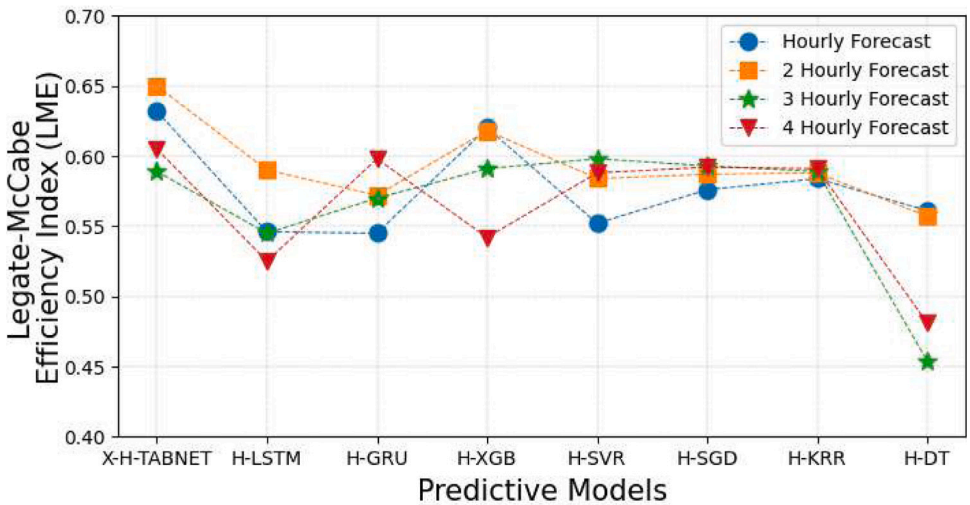

Fig. 6. Line graphs of Legate-McCabe Efficiency Index (*LME*), for the proposed X-H-TabNet model against its comparative counterparts during the testing phase at multiple time scales.

the slope m represents the gradient for a 1:1 correlation, R^2 measures the covariance, and the intercept c indicates the y-axis intercept, which should be negligible for an ideal forecasting model. The X-H-TabNet model demonstrates superior performance compared to the other models. Specifically, the X-H-TabNet model achieved $m = 0.731$, $c = 31.252$, and $R^2 = 0.824$, surpassing the performance of the H-LSTM model ($m = 0.708$, $c = 18.765$, $R^2 = 0.783$), the H-GRU model ($m = 0.708$, $c = 18.765$, $R^2 = 0.730$), and the H-XGB model ($m = 0.827$, $c = 21.162$, $R^2 = 0.796$). These findings clearly indicate that the X-H-TabNet model exhibits a better capability to accurately simulate *UV-B* radiation, as evidenced by the higher R^2 values. The superior gradient and intercept values further affirm the model's robustness and precision in capturing the underlying patterns and dependencies in the *UV-B* data. Consequently, the X-H-TabNet model stands out as a highly effective tool for *UV-B* prediction, demonstrating advanced predictive capabilities and reliable accuracy in various forecasting horizons.

Fig. 8 illustrates the frequency distribution of absolute forecasting errors for the X-H-TabNet model compared to the H-LSTM, H-GRU, H-XGB, H-SVR, H-SGD, H-KRR, and H-DT models during the testing phase. Additionally, the figure presents the percentage of each hour in the testing period with an error level within the range of ±10. The X-H-TabNet model demonstrated the highest frequency of forecasting errors within the smallest error range (±10), achieving 70%. This performance is significantly superior to the error frequencies of 63%, 63%, 66%, 66%, 64%, 66%, and 60% achieved by the H-LSTM, H-GRU, H-XGB, H-SVR, H-SGD, H-KRR, and H-DT models, respectively. This notable result indicates that the X-H-TabNet model consistently produced lower forecasting errors in comparison to the other models. The higher percentage of errors within the ±10 range underscores the model's enhanced accuracy and reliability in forecasting *UV-B* radiation. Thus, the X-H-TabNet model's overall performance in the testing phase is markedly better, as evidenced by the lower absolute forecasting errors.

To analyze local explanations for predictions made by a hybrid explainable model, this study employed the LIME framework. The number of LIME-explainable instances were equivalent to the number of *UV-B* data points for each forecast horizon (*i.e.*, hourly, 2 hourly, 3 hourly and 4 hourly) in the testing datasets. Fig. 9 visually presents the LIME-generated analyses for instance-based predictions, specifically highlighting instances 50 and 100. The bar graphs illustrate the contributions of individual features to the forecasting of these instances across four forecast horizon. Features are depicted on the $y-axis$ with their corresponding values, while the $x-axis$ indicates the relative strengths of these features in numerical terms. Features that positively influenced the *UV-B* forecast are marked in green, whereas those with a *UV-B* negative impact are highlighted in red. Fig. 9(a) illustrates the contributions of various features to the X-H-TabNet predictions for Instance 50 (left) and Instance 100 (right) for an hourly forecast horizon. In both instances, UVB(t-6) ≤ 76.16 has the most significant negative impact, indicating its consistent influence. Other features such as UVB(t-1) ≤ 76.16 and UVB(t-5) ≤ 76.16 also show substantial negative contributions across both instances. For positive influences, 76.16 < UVB(t-1) ≤ 135.84 for Instance 50 and 76.16 < UVB(t-3) ≤ 135.84 for Instance 100 are top contributors, although specific thresholds differ slightly. Features like TCO ≤ 263.60 and 42.26 < SZA ≤ 52.23 for Instance 50, and 76.16 < UVB(t-4) ≤ 135.84 and −25.60 < PCA1 ≤ −21.77 for Instance 100, show positive contributions with varying magnitudes. Features like PCA3 > 33.79 and PCA4 ≤ −11.97 negatively impact both instances, with varying influence. Unique features include DE > 0.01 positively influencing Instance 50 and TAAP >

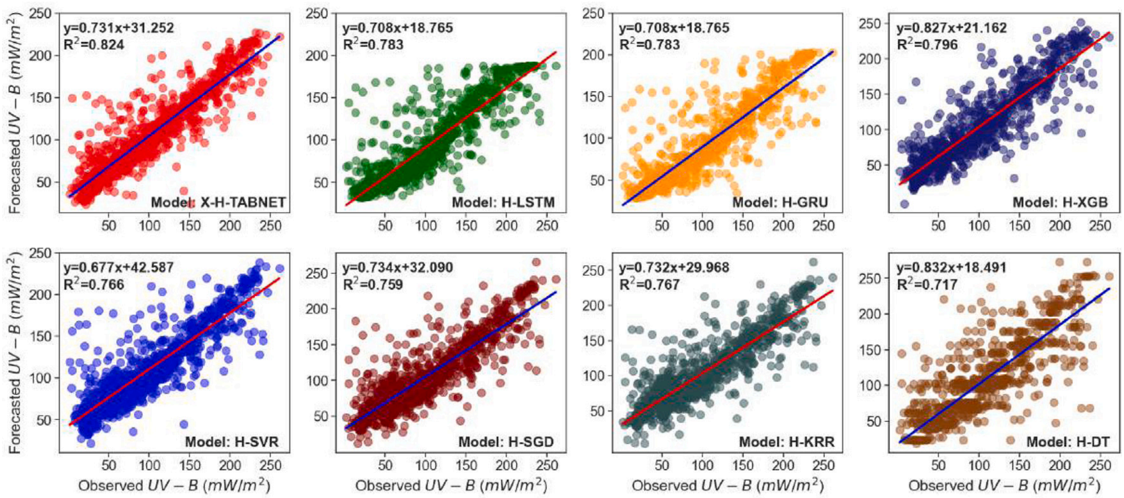

Fig. 7. Scatterplots of the observed and forecasted *UV-B* data for the optimal X-H-TabNet framework against the benchmarked models in the testing phase for 1 h forecast horizon. The coefficient of determination (R^2) and equations of linear regression are displayed in each panel.

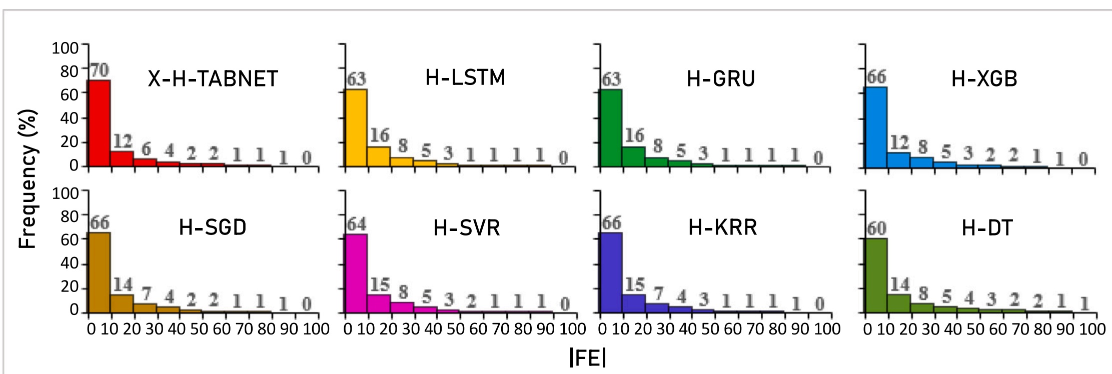

Fig. 8. Histogram displaying the aggregated percentage frequency of absolute forecasted errors (|FE|) for the superior performing X-H-TabNet model against the competing counterparts in predicting *UV-B* radiation during the testing phase.

0.72 negatively impacting Instance 100. Similarly, for the two-hourly forecast horizon shown in Fig. 9(b), UVB(t-6) ≤ 76.16 consistently has the most significant negative impact. Other features like UVB(t-5) ≤ 76.16 and TPWV ≤ 15.20 also show substantial negative contributions. For positive influences, 42.26 < SZA ≤ 52.23 for Instance 50 and SZA > 52.23 for Instance 100 are top contributors. Features like 76.16 < UVB(t-1) ≤ 135.84 for Instance 50 and 76.16 < UVB(t-2) ≤ 135.84 for Instance 100 show positive contributions with varying magnitudes. Features like PCA4 ≤ −12.22 and PCA2 ≤ −28.81 negatively impact both instances with varying influence. Unique features include DE > 0.01 positively influencing Instance 50 and TAAP > 0.72 negatively impacting Instance 100.

Additionally, in Fig. 9(c), for the three-hour forecast horizon, UVB(t-4) ≤ 76.16 has the most significant negative impact on Instance 50, while SZA ≤ 52.23 has the most significant positive impact on Instance 100. Other negatively influential features include 42.26 < SZA ≤ 52.23 and UVB(t-6) ≤ 76.16 for Instance 50, and UVB(t-1) ≤ 76.16 and UVB(t-6) ≤ 76.16 for Instance 100. Positive influences for Instance 50 include 76.16 < UVB(t-1) ≤ 135.84 and DE > 0.01, while for Instance 100, 76.16 < UVB(t-4) ≤ 135.84 and TPWV ≤ 15.19 are significant. Common features with varying impacts include PCA2 ≤ −28.76 and PCA4 ≤ −12.12. Lastly, in Fig. 9(d), for the four-hour forecast horizon, UVB(t-3) ≤ 76.16 has the most significant negative impact on Instance 50, while 76.16 < UVB(t-3) ≤ 135.84 is the most significant negative feature for Instance 100. Other negatively influential features include UVB(t-4) ≤ 76.16 and UVB(t-5) ≤ 76.16 for Instance 50, and 76.16 < UVB(t-4) ≤ 135.84 and UVB(t-5) ≤ 76.16 for Instance 100. Positive influences for Instance 50 include 42.26 < SZA ≤ 52.23 and PCA2 ≤ −28.96, while for Instance 100, UVB(t-6) ≤ 76.16 and TPWV ≤ 15.19 are significant. Common features with varying impacts include SZA ≤ 52.23 and PCA2 ≤ −28.96. Overall, all local explanation charts (Fig. 9) reveal a mix of common and unique feature impacts, demonstrating the X-H-TabNet model sensitivity to different factors across 50th and 100th instances. The consistent features across instances indicate their robust influence, while the varying features highlight the model's adaptability to different data scenarios.

Additionally, to derive global explanations for the predictions generated by the X-H-TabNet model, this study utilized a conventional SHAP model-agnostic framework. The SHAP summary beeswarm plots for four forecasting horizons illustrate significant patterns in feature importance and their effects on model predictions (see Fig. 10). Across all horizons, certain features like the lagged component of *UV-B* (e.g., UVB(t-6)), SZA, and PCA components consistently emerge as significant contributors. For instance, UVB(t-6) is prominently influential across all plots, although its impact magnitude decreases as the forecasting horizon extends, indicating a stronger influence in the short term. There are noticeable shifts in the ranking and influence of features over different horizons. For example, SZA has a substantial impact in the 2-h forecast (Fig. 10b) but its influence reduces in the 1-h (Fig. 10a) and 3-h (Fig. 10c) horizons, and it appears even less significant in the 4-h forecast (Fig. 10d). Similarly, the feature DE is impactful in the 2-h (Fig. 10b) and 3-h (Fig. 10c) forecasts but less so in the 1-h (Fig. 10a)

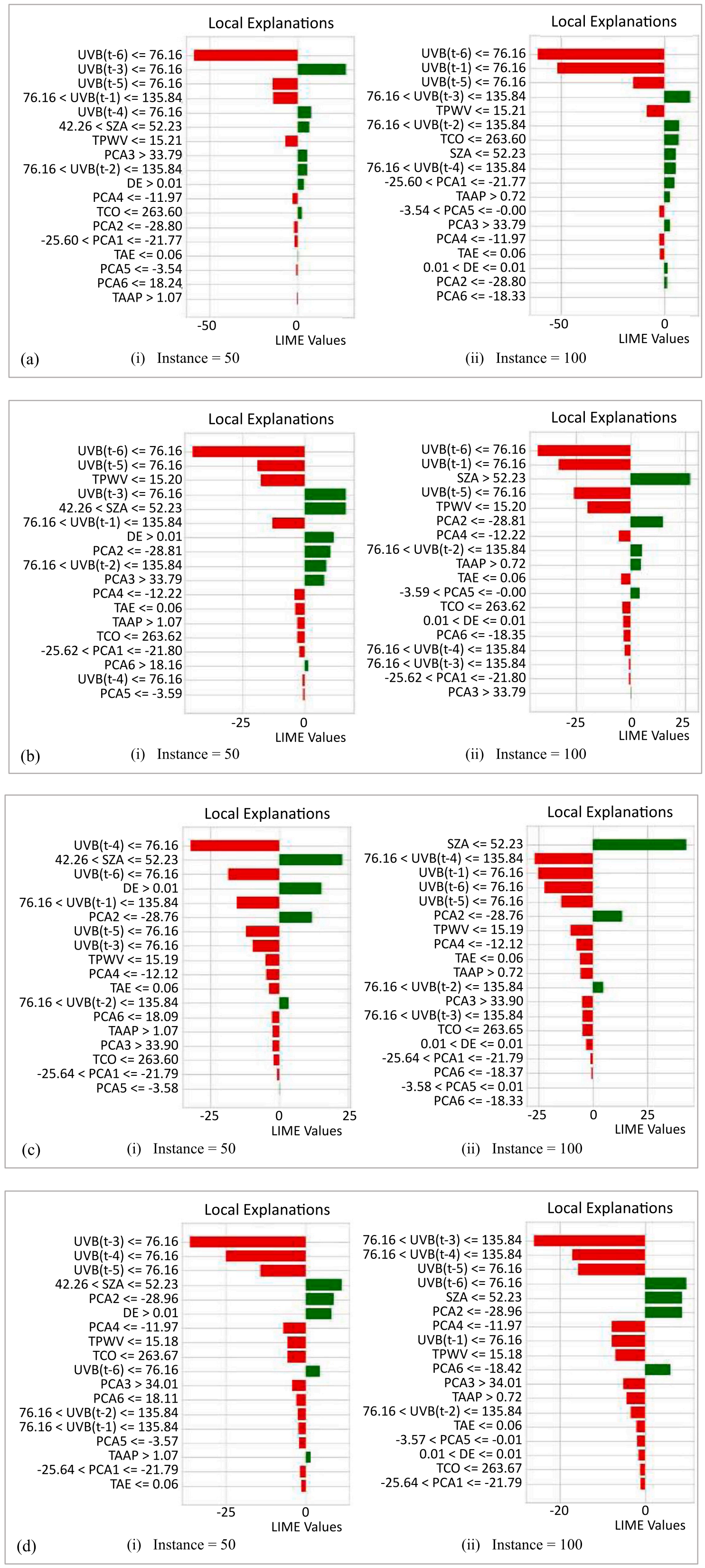

Fig. 9. LIME explanation bar plots at (i) instance 50 and (ii) instance 100 for the forecast horizon (a) 1 h, (b) 2 h, (c) 3 h and (d) 4 h, where the red bars indicate that the predictor variables have a negative influence on the model (minimize the model score) and the green bars indicate that the predictor variables have a positive influence on the model (maximize the model score).

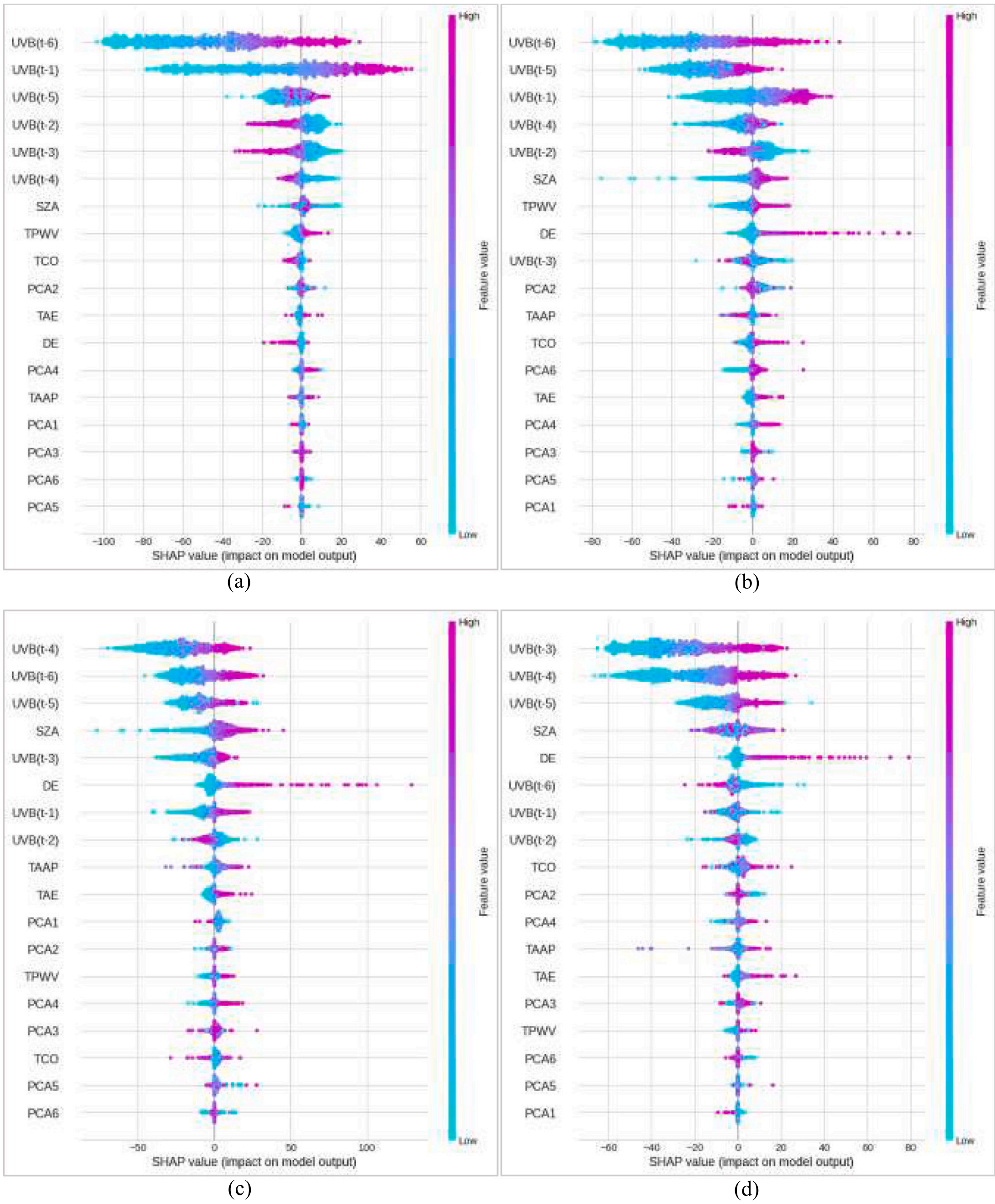

Fig. 10. SHAP summary beeswarm plots for the forecast horizons (a) 1 h, (b) 2 h, (c) 3 h and (d) 4 h.

and 4-h (Fig. 10d) forecasts, demonstrating temporal variability in its relevance. The density and distribution of SHAP values, depicted by the beeswarm plots, indicate the spread and variance of each feature's impact. For instance, UVB(t-6) has a wider spread in the 1-h forecast (Fig. 10a), suggesting more variability in its influence compared to a more concentrated spread in the 4-h forecast (Fig. 10d). This variability is further highlighted by the color gradient (cyan to magenta), which represents feature values from low to high, showing how high or low values of a feature influence the prediction. High values of UVB(t-6), for example, generally have a positive impact, whereas low values may have a negative impact. Overall, these SHAP summary plots demonstrate the dynamic nature of feature importance across different forecasting horizons. While some features like the lagged component of *UV-B* maintain consistent importance, their impact diminishes over longer horizons. The varying levels of influence for features like SZA and DE underscore the temporal dependency of their importance, providing a nuanced understanding of how different features contribute to model predictions over time.

The SHAP dependence plots presented in Fig. 11 elucidate the marginal effects of two attributes on the predicted outcomes of the hybrid explainable X-H-TabNet model. In this study, these plots are utilized to investigate the interactions between the most influential predictor variables during the testing phase. Specifically, for the 1-h forecast horizon, the interactions between UVB(t-6) and UVB(t-1) are explored. For the 2-h horizon, UVB(t-5) and UVB(t-6) are examined, and similarly, for the 3-h horizon, the same pair of predictors (UVB(t-5) and UVB(t-6)) are analyzed. Finally, for the 4-h horizon, the interactions between UVB(t-4) and UVB(t-3) are considered. These analyses provide insight into how these critical predictors influence the model's prediction outcomes across different forecasting horizons.

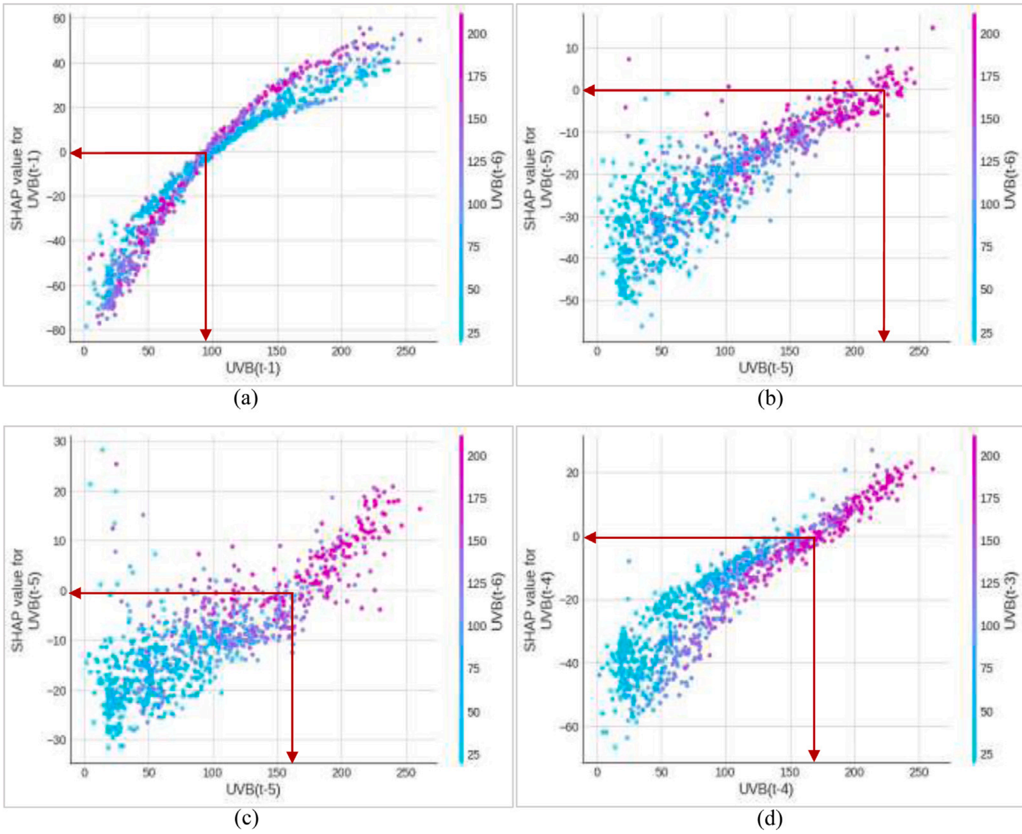

Fig. 11. SHAP dependence plots showing interactions between various lags of PACF, which are the most significant predictors in the *UV-B* forecasting system for the forecast horizons (a) 1 h, (b) 2 h, (c) 3 h and (d) 4 h.

For the hourly forecast horizon, depicted in Fig. 11(a), the interaction between UVB(t-1) and UVB(t-6) is examined. The SHAP values for UVB(t-1) show a positive correlation with its values, indicating that higher values of UVB(t-1) correspond to higher impacts on the model output. The predicted values of *UV-B* are more likely to be favored when UVB(t-1) is less than or equal to 100 and UVB(t-6) values are high. In the two-hourly forecast horizon, shown in Fig. 11(b), the interaction between UVB(t-5) and UVB(t-6) is highlighted. The SHAP values for UVB(t-5) also display a positive correlation, although with a broader spread compared to the 1-h forecast. This suggests that UVB(t-5) remains an important predictor, but its influence is slightly more variable. Additionally, the predicted values of *UV-B* are more likely to be favored when UVB(t-5) is less than or equal to 225 and UVB(t-6) values are high.

For the three-hourly forecast horizon, illustrated in Fig. 11(c), the plot focuses on the interaction between UVB(t-5) and UVB(t-6), similar to the 2-h forecast. The SHAP values for UVB(t-5) display a more complex relationship, with some variability and a generally positive trend. This indicates a consistent but slightly less stable impact of UVB(t-5) over this horizon. Furthermore, the predicted values of *UV-B* are more likely to be favored when UVB(t-5) is less than or equal to 160 and UVB(t-6) values are high. In the four-hourly forecast horizon, depicted in Fig. 11(d), the plot shows the interaction between UVB(t-4) and UVB(t-3). The SHAP values for UVB(t-4) demonstrate a positive correlation, similar to the previous horizons. However, the relationship is more linear and less dispersed, suggesting a stable and significant influence of UVB(t-4) for longer forecasting periods. Moreover, the predicted values of *UV-B* are more likely to be favored when UVB(t-4) is less than or equal to 170 and UVB(t-3) values are high.

The SHAP dependence plots provide critical insights into the significance and interaction of specific solar *UV-B* radiation lags across varying forecast horizons. For shorter forecast periods, such as the one-hour and two-hour horizons, the predictors UVB(t-1) and UVB(t-5) exhibit strong positive correlations with their SHAP values. This suggests a substantial impact on the model output, albeit with some variability. These predictors are pivotal in driving the forecast accuracy for these shorter horizons. As the forecasting horizon extends to three and four hours, the predictors UVB(t-5) and UVB(t-4) continue to demonstrate their importance. Specifically, in the three-hour forecast, UVB(t-5) maintains its significant influence, though with a slightly more complex relationship. For the four-hour forecast horizon, UVB(t-4) emerges as a key predictor, showing a stable and linear relationship with its SHAP values. This linearity indicates a more consistent and reliable impact on the model output over longer periods. These observations underscore the dynamic and temporal nature of the *UV-B* forecasting system. The varying degrees of impact of specific *UV-B* lags across different time horizons highlight the model's sensitivity to temporal dependencies. Understanding these interactions is crucial for enhancing the predictive performance and reliability of *UV-B* forecasts. Such insights can guide the refinement of forecasting models, ensuring they are tailored to capture the nuanced influences of lagged features of *UV-B*.

Aerosols are also known to be the potential influential features that impact solar UV radiation (Campanelli et al., 2019), particularly the *UV-B* component for this study. The aerosol effects include the influence of suspended particulate matter (such as $PM_{2.5}$) and other dust particles in the atmosphere. This study investigated the contributions of aerosol interactions towards *UV-B* predictions using the predictor variables of TAE, TAAP and DE. In accordance with Fig. 9(a)–(d), the LIME plots at Instance 50 of 1-h forecast horizon show that TAE $\leq$ 0.06, and TAAP $>$ 1.07 contribute negatively towards *UV-B* predictions, while DE $\geq$ 0.06 contributes positively. At instance 100, TAAP $>$ 0.72 shows negative contributions, while TAE $\leq$ 0.06 and DE $\geq$ 0.01 provides positive influence. In a similar manner, these atmospheric variables (representing aerosol and dust particles) also show significant positive and negative contributions towards *UV-B* predictions at 2-h, 3-h and 4-h forecast horizons. In the case of SHAP plots illustrated in Fig. 10(a)–(d), aerosols and dust particles, again depicted by the variables of TAE, TAAP and DE also provide some significant contributions towards *UV-B* predictions at all the forecast horizons. Overall, the analysis of the contributions of aerosols (particulate matter and dust) using LIME and SHAP plots indicate their moderate to low contributions towards *UV-B* predictions. In such situations, pollution levels may align more closely with light to moderate pollution episodes. However, further studies can be conducted to reconfirm the classifications of aerosol contributions into different pollution levels.

Toowoomba is located in a regional location 110 km west of the Pacific Ocean and state capital of Brisbane. The Toowoomba measurement site experiences a clean atmosphere with minimal contribution from anthropogenic pollutants. Mineral dust and smoke particulate matter contribute to the absorption of solar *UV-B* radiation measured by the 501-Biometer. The contribution of local aerosol was evaluated for the year 2003, using cloud-free solar noon *UV-A* spectra measured by the University of Southern Queensland's DTM300 spectroradiometer (Bentham Instruments, Reading, UK). This instrument records the solar spectral UV at 0.5 nm increments between 280 to 400 nm at 10 min intervals daily (Parisi and Downs, 2004). A total of 12 cloud-free noon *UV-A* spectra recorded between 315 and 400 nm were available for comparison to the tropospheric ultraviolet and visible (TUV) Radiative Transfer code described by Madronich and Flocke (1998) and available online at https://www.acom.ucar.edu/Models/TUV/Interactive_TUV/. Comparison of the measured to modeled *UV-A* (a measurement independent ozone concentration) taken at solar noon under cloud free conditions was made according to the recent method described by McKenzie et al. (2022) to derive the average extinction of *UV-A* radiation at the measurement site due to local aerosols. For 2003, the measured to modeled *UV-A* ratio averaged 0.96 ± 0.025 (1 s.d.), indicating the Toowoomba site has a relatively clean atmosphere, a little poorer that Lauder (New Zealand) at 0.98 but better than other notable UV radiation measurement sites including Alice Springs, Australia at 0.91 and Boulder, Colorado USA at 0.90 (McKenzie et al. 2022). Given extinction of the solar *UV-A* in Toowoomba averaged 4% for the year 2003 due to local aerosols, measurement variations of the erythemal UV reported here are most likely to be affected by cloud and total column ozone. *UV-A* radiation has been utilized in this regard to assess the contribution of aerosol as the *UV-A* spectrum is not influenced by ozone concentration. This provides insight into the anticipated attenuation of *UV-B* irradiance due to the presence of aerosol in the current study. For instance, if the *UV-A* is attenuated by 4% on average, it is safe to assume that *UV-B* is also attenuated by 4%, as particulate matter and aerosols scatter and absorb light evenly across all wavelengths.

Our research has implemented *xAI* tools in response to the heightened demand for explaining black-box model predictions and achieving trustworthy AI. Earlier studies mostly indicated that AI predictive tools were of high precision, but they lacked the ability to explain black-box model outcomes (Holzinger, 2021; Holzinger et al., 2022). Small perturbations in the input data can significantly influence the output, undermining robustness and leading to completely different results. Largely, the issue arises from poor data quality due to a lack of expected independent and identically distributed (i.i.d.) datasets (Holzinger, 2021). Additionally, it is essential to address ethical and legal aspects to ensure all AI-derived solutions meet ethical and legal norms (Holzinger et al., 2022). The explainability and robust execution of AI models foster confidence and high-performance reliability, empowering human experts to maintain control over the AI-pipeline with assurance. Our study acknowledges the aforementioned mandatory needs in the *UV-B* forecasting system and implemented trustworthy AI by integrating brilliant model-agnostic *xAI* tools with the hybridized TabNet model.

Given the improved performance and capacity to deliver explainable results, we further demonstrate the practical application of the multiple input multi-step output *UV-B* forecasting framework in Fig. 12. The newly developed decision support tool operates in online and offline settings to provide multi-step *UV-B* exposure risk information to the expert end-users in implementing sun-protection. For effective delivery of *UV-B* forecasts, the online pre-trained X-H-TabNet is largely dependent on the offline updated X-H-TabNet system. In light of this, the prescribed model is first trained and optimized via the offline platform, integrating updates of newly labeled datasets accessed from existing databases such as UniSQ's atmoSEQ (mdVine, 2024).

Periodically, the updated model from the offline setup can replace the pre-trained online model to ensure more accurate and trustworthy forecasting performance. Through the user-interface, the online platform can offer more accurate forecasts of *UV-B* at multi-step horizons in terms of model performance aptitudes of *r*, *MAE*, *RMSE* and *LME*. Additionally, the user interface can offer explanations that are model-agnostic, designed to enhance the reliability and trustworthiness of predictions across local and global levels. Overall, analyzing the outputs from the user interphase can aid the experts and end users (ideally, specialists in solar UV radiation, forecasters or users with an interest in knowing the *UV-B* ahead of time) to deliver more accurate sun-exposure recommendations for the protection of people and terrestrial life at risk of harmful exposure to *UV-B* radiation.

Currently, solar *UVI* information is provided to the public through daily forecasts or warnings. Such forecasts often provide the erythema *UV-B* irradiance as the daily maximum *UVI* expected under a cloud-free sky (where the *UVI* may be calculated as the erythema *UV-B* divided by 25 mW m^{-2}). Practical advice published by the WHO in 2002 (World Health Organization, 2002) recommends sun protection strategies be implemented when the *UVI* reaches 3 or more (75 mW m^{-2}). For Southern Queensland, our dataset, recorded between July 2002 and February 2004 shows there are significant seasonal but also short-term influences on the potentially harmful *UV-B*.

In our case, the *UV-B* readily exceeded 300 mW m^{-2} (*UVI* 12). This represents an extreme solar *UV* irradiance and as shown here, was the measured *UV-B* irradiance that can occur under cloud-affected skies 2. Our method, utilizing the proposed X-H-TabNet system has been shown to make accurate predictions of the *UV-B* from datasets collected under real-time stochastic conditions for a range of hourly horizons. Under cloud-affected skies, rapid fluctuations in the surface *UV-B* can occur and persist for minutes, hours and extended periods of time during the day. Overcast sky conditions will often reduce the forecast *UV-B* for extended periods (Aun et al., 2011). On occasion broken cumulus cloud cover can even elevate the *UV-B* above predicted cloud-free levels (Sabburg and Calbó, 2009). To be able to predict *UV-B* in advance over hourly or extended hourly horizons has clear benefit to the research community.

5. Conclusions and future work

The paper reports the key merits and performance effectiveness of the explainable hybrid X-H-TabNet model for short-term solar *UV-B* predictions across multiple forecast horizons. The proposed model was validated using satellite and ground data from Queensland, Australia, where *UV-B* exposure is notably high and poses risks to people, animals, and plants.

In the quest for boosting the performance of the newly proposed model and reducing the computational costs, effective dimensionality reduction was performed using RFECV algorithm and principal component analysis. Further performance enhancement was achieved by fine tuning the TabNet architecture using Optuna algorithm. Rigorous benchmarking of the objective hybrid TabNet model, designated as X-H-TabNet, with other competing counterparts of H-LSTM, H-GRU,

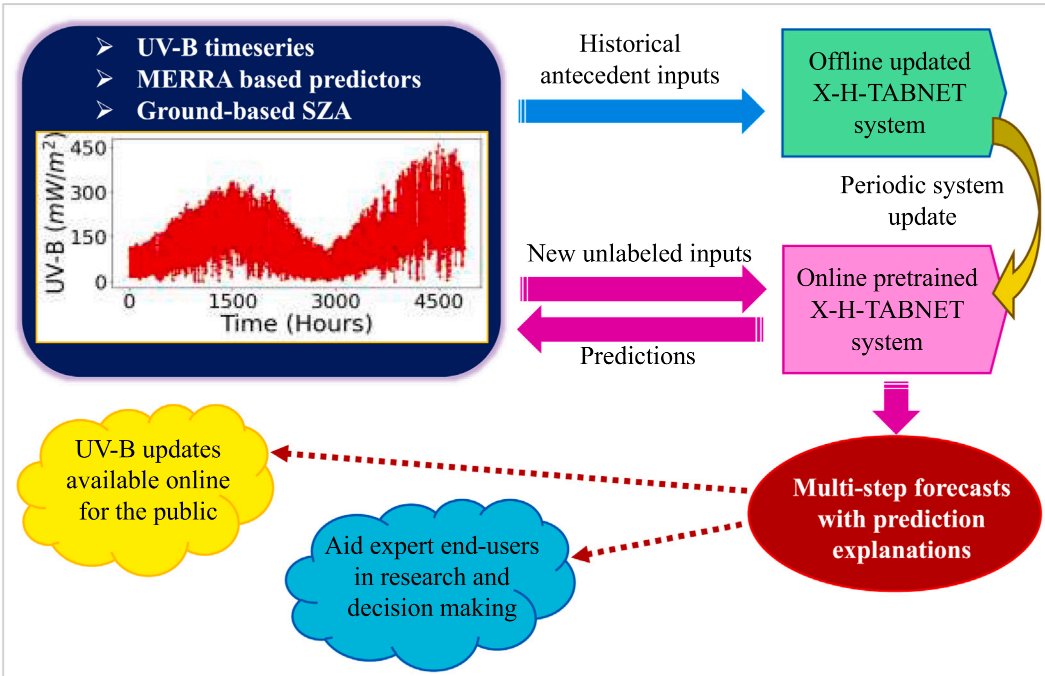

Fig. 12. Schematic diagram detailing the real-life application of the online and offline explainable hybrid X-H-TabNet system in generating short-term forecasts of *UV-B* radiation at multiple time scales.

H-XGB, H-SVR, H-SGD, H-KRR and H-DT with several statistical score metrics and diagnostic plots elucidate superior predictive performance by the proposed objective model.

The evaluation outcomes of *UV-B* forecasts reveal that the newly proposed model achieved comparatively high correlation coefficients (r) of 0.908 at hourly horizon, 0.880 at 2-hourly horizon, 0.868 at 3-hourly horizon, and 0.868 at 4-hourly horizon. Assessment with Legates and McCabe's index (*LME*) further confirm the performance superiority of the objective model. In terms of the error values, the objective model captured the lowest Root Mean Squared Error (*RMSE*) and Mean Absolute Error (*MAE*) for almost all the four forecast horizons. Exploitation of the *xAI* tools of LIME and SHAP with the proposed TabNet model highlight the significant contributions of the entire feature sets in generating predictions of *UV-B* radiation. In accordance with the combined local and global model-agnostic outcomes of LIME and SHAP tools, the antecedent lagged memory of *UV-B* and the solar zenith angle were observed to contribute significantly towards the model predictions. The feature attributes associated with ozone and cloud cover effects were also impactful in predicting *UV-B* radiation.

By offering reliable and interpretable short-term *UV-B* forecasts, the newly designed model can support the health sector in making informed decisions and providing the public with more accurate information on *UV-B* exposure risks, potentially reducing the incidence of skin diseases such as malignant keratinocyte cancers. Furthermore, the predictive model can provide more accurate *UV-B* forecasts for remote locations where plant and animal life thrive, thereby supporting researchers and decision-makers in exploring the impacts of *UV-B* on ecosystems. By leveraging satellite-derived datasets during model training, which integrated factors such as cloud cover, aerosols, and ozone, we affirm the real-world applicability of our *UV-B* forecasting model under intermittent cloud conditions in other temperate countries as well.

The focus of this work on short-term solar *UV-B* forecasting, rather than long-term trend analysis, suggests that future research might consider retraining the prescribed X-H-TabNet model with long-term data. These datasets could encompass solar radiation, air temperature, and other atmospheric variables (e.g., visibility) to evaluate the model's forecasting abilities over longer horizons like months or seasons, if such long-term predictions are deemed significant. Moreover, the uncertainty in sky images data and satellite products can also affect the prediction of *UV-B* radiation. However, the current research investigations were not focused on quantifying such uncertainties. We acknowledge this research limitation as an area that needs to be explored more comprehensively in the near future.

Cloud modification factors (CMF) based upon the sky conditions and the cloud type remain an area of active research. Our newly proposed X-H-TabNet model trained using known cloud cover type and conditions could be utilized to classify the probability of enhancements or reductions in the solar *UV-B*. Given forecasts provided to the public do not take cloud cover effects into account, the potential for improved characterization of the *UVI* is potentially significant, especially given that certain broken cloud cover conditions can enhance the *UV-B* by more than 20% of the expected cloud-free *UV-B* (Sabburg and Calbó, 2009). How long such events last, their frequency and likelihood of occurrence can all be evaluated using X-H-TabNet.

In this research we train X-H-TabNet on a single *UV-B* dataset that extended over 18 months between July 2002 and February 2004. Similar methods employed to trained *UV-B* models for high risk summertime conditions at sites located in different parts of Queensland or wider Australia may yield information that could be utilized for local predictions in densely populated centers, including Sydney and Brisbane (locations of known high melanoma skin cancer incidence Cramb et al., 2020). Variability in the *UV-B* due to changes in the climate might also be examined using a larger dataset including atmoSEQ (mdVine, 2024) or other publicly accessible *UV* datasets such as the real-time Australian Radiation and Nuclear Safety Authority (ARPANSA) *UV-B* network (Australian Radiation and Nuclear Safety Authority, 2024). In addition, ERA-5 datasets that provide high-resolution information on meteorological variables can also be explored in future studies to enhance the forecasting capabilities of *UV-B* predictive models.

Table A.1
List of acronyms.

Acronym	Definition
ADF	Augmented Dickey–Fuller
AI	Artificial Intelligence
ANN	Artificial Neural Network
API	Application Programming Interface
CEEMDAN	Complete Ensemble Empirical Mode Decomposition with Adaptive Noise
C-LSTM	Convolution Neural Network And Long Short-Term Memory
CNN	Convolution Neural Network
DL	Deep Learning
DNN	Deep Neural Network
DT	Decision Tree
ELM	Extreme Learning Machine
FS	Feature Selection
GIOVANNI	Goddard Online Interactive Visualization and Analysis Infrastructure
GLU	Gated Linear Unit
GPU	Graphics Processing Unit
GRU	Gated Recurrent Unit
KRR	Kernel Ridge Regression
LIME	Local Interpretable Model-Agnostic Explanations
LME	Legate-Mccabe's Efficiency Index
LSTM	Long Short-Term Memory
MAE	Mean Absolute Error
MARS	Multivariate Adaptive Regression Splines
MERRA-2	Modern-Era Retrospective Analysis for Research and Applications
ML	Machine Learning
MLP	Multilayer Perceptrons
NASA	National Aeronautics and Space Administration
PACF	Partial Autocorrelation Function
PCA	Principal Component Analysis
PCs	Principal Components
PSO	Particle Swarm Optimization
r	Pearson's Correlation Coefficient
RBR	Red-Blue Ratio
RFECV	Recursive Feature Elimination with Cross-Validation
ReLU	Rectified Linear Unit
RF	Random Forest
RMSE	Root Mean Squared Error
SGD	Stochastic Gradient Descent
SHAP	SHapley Additive exPlanations
SVR	Support Vector Regression
SZA	Solar Zenith Angle
TSI	Total Sky Imager
UV	Ultraviolet
UV-A	Ultraviolet Radiation in Category A
UV-B	Ultraviolet Radiation in Category B
UVI	Ultraviolet Index
xAI	Explainable Artificial Intelligence
XGB	Extreme Gradient Boosting

CRediT authorship contribution statement

Salvin S. Prasad: Writing – original draft, Visualization, Validation, Software, Methodology, Investigation, Funding acquisition, Formal analysis, Data curation, Conceptualization. **Lionel P. Joseph:** Writing – original draft, Resources, Methodology, Investigation. **Sujan Ghimire:** Writing – review & editing, Visualization, Software. **Ravinesh C. Deo:** Writing – review & editing, Validation, Supervision, Resources, Project administration. **Nathan J. Downs:** Writing – review & editing, Writing – original draft, Visualization, Validation, Supervision, Software. **Rajendra Acharya:** Writing – review & editing. **Zaher M. Yaseen:** Writing – review & editing.

Declaration of competing interest

The authors declare that they have no known competing financial interests or personal relationships that could have appeared to influence the work reported in this paper.

Acknowledgments

This research did not receive any specific grant from funding agencies in the public, commercial, or not-for-profit sectors. The sky images and solar UV radiation data were acquired through the Toowoomba-based experimental research facility at the University of Southern Queensland in Australia.

Appendix. List of acronyms

See Table A.1.

Data availability

The authors do not have permission to share data.

References

Abadi, M., Agarwal, A., Barham, P., Brevdo, E., Chen, Z., Citro, C., Corrado, G.S., Davis, A., Dean, J., Devin, M., et al., 2016. Tensorflow: Large-scale machine learning on heterogeneous distributed systems. arXiv preprint arXiv:1603.04467.

Abdolrasol, M.G., Hussain, S.S., Ustun, T.S., Sarker, M.R., Hannan, M.A., Mohamed, R., Ali, J.A., Mekhilef, S., Milad, A., 2021. Artificial neural networks based optimization techniques: A review. Electronics 10 (21), 2689.

Adam, M.E.-N., Ahmed, E.A., 2016. Comparative analysis of cloud effects on ultraviolet-b and broadband solar radiation: Dependence on cloud amount and solar zenith angle. Atmos. Res. 168, 149–157.

Ahmed, A.M., Ahmed, M.H., Saha, S.K., Ahmed, O., Sutradhar, A., 2022. Optimization algorithms as training approach with hybrid deep learning methods to develop an ultraviolet index forecasting model. Stoch. Environ. Res. Risk Assess. 36 (10), 3011–3039.

Akiba, T., Sano, S., Yanase, T., Ohta, T., Koyama, M., 2019. Optuna: A next-generation hyperparameter optimization framework. In: Proceedings of the 25th ACM SIGKDD International Conference on Knowledge Discovery & Data Mining. pp. 2623–2631.

Alresheedi, A.A., Al-Hagery, M.A., 2020. Forecasting the global horizontal irradiance based on boruta algorithm and artificial neural networks using a lower cost. Int. J. Adv. Comput. Sci. Appl. 11 (9).

Alsina, E.F., Bortolini, M., Gamberi, M., Regattieri, A., 2016. Artificial neural network optimisation for monthly average daily global solar radiation prediction. Energy Convers. Manage. 120, 320–329.

Arik, S.Ö., Pfister, T., 2021. Tabnet: Attentive interpretable tabular learning. In: Proceedings of the AAAI Conference on Artificial Intelligence. Vol. 35, pp. 6679–6687.

Aun, M., Kalju, E., Ansko, I., Veismann, U., Lätt, S., 2011. Modification of spectral ultraviolet doses by different types of overcast cloudiness and atmospheric aerosol. Photochem. Photobiol. 87, 461–469.

Australian Radiation and Nuclear Safety Authority, 2024. Ultraviolet radiation index. https://www.arpansa.gov.au/our-services/monitoring/ultraviolet-radiation-monitoring/ultraviolet-radiation-index. [Online]; (Accessed 23 July 2024).

Awad, M., Fraihat, S., 2023. Recursive feature elimination with cross-validation with decision tree: Feature selection method for machine learning-based intrusion detection systems. J. Sens. Actuator Netw. 12 (5), 67.

Balalla, D.T., Nguyen-Huy, T., Deo, R., 2021. MARS model for prediction of short-and long-term global solar radiation. In: Predictive Modelling for Energy Management and Power Systems Engineering. Elsevier, pp. 391–436.

Berrick, S.W., Shen, S., Ostrenga, D., 2008. Modern era retrospective restrospective-analysis for research and applications (MERRA) data and services at the GES DISC. In: American Geophysical Union Meeting.

Bilbao, J., Miguel, A., 2013. Contribution to the study of UV-B solar radiation in Central Spain. Renew. Energy 53, 79–85.

Borghini, E., Giannetti, C., 2021. Short term load forecasting using TabNet: A comparative study with traditional state-of-the-art regression models. Eng. Proc. 5 (1), 6.

Brahma, P.P., Wu, D., She, Y., 2015. Why deep learning works: A manifold disentanglement perspective. IEEE Trans Neural Netw. Learn. Syst. 27 (10), 1997–2008.

Campanelli, M., Siani, A.M., di Sarra, A., Iannarelli, A.M., Sanò, P., Diémoz, H., Casasanta, G., Cacciani, M., Tofful, L., Dietrich, S., 2019. Aerosol optical characteristics in the urban area of Rome, Italy, and their impact on the UV index. Atmospheric Meas. Tech. Discuss. 2019, 1–23.

Chang, N.-B., Feng, R., Gao, Z., Gao, W., 2010. Skin cancer incidence is highly associated with ultraviolet-B radiation history. Int. J. Hyg. Environ. Health 213 (5), 359–368.

Chen, Z.-Y., Zhang, T.-H., Zhang, R., Zhu, Z.-M., Yang, J., Chen, P.-Y., Ou, C.-Q., Guo, Y., 2019. Extreme gradient boosting model to estimate PM2. 5 concentrations with missing-filled satellite data in China. Atmos. Environ. 202, 180–189.

Cherrie, J.W., Cherrie, M.P., 2022. Workplace exposure to UV radiation and strategies to minimize cancer risk. Br. Med. Bull. 144 (1), 45–56.

Commission Internationale de l'Eclairage, 1998. Erythema Reference Action Spectrum and Standard Erythema Dose. CIE S 007/E:1998 , ISO 17166:1999.

Coussens, A.K., et al., 2017. The role of UV radiation and vitamin D in the seasonality and outcomes of infectious disease. Photochem. Photobiol. Sci. 16 (3), 314–338.

Cramb, S.M., Duncan, E.W., F, A.J., P, S.H., L, M.K., D, B.P., 2020. Geographical patterns in melanoma incidence across Australia: can thickness differentials reveal the key drivers? Ann. Cancer Epidemiology 4 (11), http://dx.doi.org/10.21037/ace--20--13.

Csintalan, Z., Tuba, Z., Takács, Z., Laitat, E., 2001. Responses of nine bryophyte and one lichen species from different microhabitats to elevated UV-B radiation. Photosynthetica 39 (2), 317–320.

Cullen, A.P., 2011. Ozone depletion and solar ultraviolet radiation: Ocular effects, a United Nations Environment Programme perspective. Eye Contact Lens: Sci. Cln. Pract. 37 (4), 185–190.

Dauphin, Y.N., Fan, A., Auli, M., Grangier, D., 2017. Language modeling with gated convolutional networks. In: International Conference on Machine Learning. PMLR, pp. 933–941.

Davis, D.S., Robinson, C., Callender, V.D., 2021. Skin cancer in women of color: Epidemiology, pathogenesis and clinical manifestations. Int. J. Women's Dermatol. 7 (2), 127–134.

De Gruijl, F.R., 2002. Photocarcinogenesis: UVA vs. UVB radiation. Skin Pharmacol. Appl. Skin Physiol. 15 (5), 316–320.

Deo, R.C., Downs, N., Parisi, A.V., Adamowski, J.F., Quilty, J.M., 2017a. Very short-term reactive forecasting of the solar ultraviolet index using an extreme learning machine integrated with the solar zenith angle. Environ. Res. 155, 141–166.

Deo, R.C., Ghimire, S., Downs, N.J., Raj, N., 2018. Optimization of windspeed prediction using an artificial neural network compared with a genetic programming model. In: Handbook of Research on Predictive Modeling and Optimization Methods in Science and Engineering. IGI Global, pp. 328–359.

Deo, R.C., Grant, R.H., Webb, A., Ghimire, S., Igoe, D.P., Downs, N.J., Al-Musaylh, M.S., Parisi, A.V., Soar, J., 2022. Forecasting solar photosynthetic photon flux density under cloud cover effects: novel predictive model using convolutional neural network integrated with long short-term memory network. Stoch. Environ. Res. Risk Assess. 36 (10), 3183–3220.

Deo, R.C., Tiwari, M.K., Adamowski, J.F., Quilty, J.M., 2017b. Forecasting effective drought index using a wavelet extreme learning machine (W-ELM) model. Stoch. Environ. Res. Risk Assess. 31, 1211–1240.

Dexter, B., King, R., Parisi, A., Harrison, S., Konovalov, D., Downs, N., 2020. Keratinocyte skin cancer risks for working school teachers: Scenarios and implications of the timing of scheduled duty periods in queensland, Australia. J. Photochem. Photobiol. B 213, 112046.

Dickey, D.A., Fuller, W.A., 1979. Distribution of the estimators for autoregressive time series with a unit root. J. Amer. Statist. Assoc. 74 (366a), 427–431.

Ekundayo, I., 2020. Optuna Optimization-Based CNN-LSTM Networks for Predicting Energy Consumption (Ph.D. thesis MS thesis). MS thesis, School Comput., Nat. College Ireland, Dublin, Ireland.

Fan, J., Wu, L., Ma, X., Zhou, H., Zhang, F., 2020. Hybrid support vector machines with heuristic algorithms for prediction of daily diffuse solar radiation in air-polluted regions. Renew. Energy 145, 2034–2045.

Feister, U., Cabrol, N., Häder, D., 2015. UV irradiance enhancements by scattering of solar radiation from clouds. Atmosphere 6 (8), 1211–1228.

Freytes, C.Y., Mayrand, R.P., Sawada, L.O., Liang, T.Y., Cid, R.E.C., Burke, S., Loewenstein, D., Duara, R., Adjouadi, M., 2023. Recursive feature elimination with cross validation for Alzheimer's disease classification using cognitive exam scores. In: 2023 Intelligent Methods, Systems, and Applications. IMSA, IEEE, pp. 327–332.

Furlan, C., De Oliveira, A.P., Soares, J., Codato, G., Escobedo, J.F., 2012. The role of clouds in improving the regression model for hourly values of diffuse solar radiation. Appl. Energy 92, 240–254.

Gao, S., Xu, J., Dan, W., Li, Q., Huang, Y., 2021. Research on optimal control of fractional order PI λ d μ parameters of SCR denitrification system. In: 2021 3rd International Conference on Industrial Artificial Intelligence. IAI, IEEE, pp. 1–6.

Garg, S., Pundir, P., 2021. Mofit: A framework to reduce obesity using machine learning and IoT. In: 2021 44th International Convention on Information, Communication and Electronic Technology. MIPRO, IEEE, pp. 1733–1740.

Gehring, J., Auli, M., Grangier, D., Yarats, D., Dauphin, Y.N., 2017. Convolutional sequence to sequence learning. In: International Conference on Machine Learning. PMLR, pp. 1243–1252.

Ghimire, S., Deo, R.C., Casillas-Pérez, D., Salcedo-Sanz, S., 2022. Boosting solar radiation predictions with global climate models, observational predictors and hybrid deep-machine learning algorithms. Appl. Energy 316, 119063.

Ghimire, S., Deo, R.C., Casillas-Pérez, D., Salcedo-Sanz, S., Pourmousavi, S.A., Acharya, U.R., 2024. Probabilistic-based electricity demand forecasting with hybrid convolutional neural network-extreme learning machine model. Eng. Appl. Artif. Intell. 132, 107918.

Ghimire, S., Deo, R.C., Downs, N.J., Raj, N., 2019. Global solar radiation prediction by ANN integrated with European Centre for medium range weather forecast fields in solar rich cities of Queensland Australia. J. Clean. Prod. 216, 288–310.

Ghoneim, A.A., Kadad, I.M., Altouq, M.S., 2013. Statistical analysis of solar UVB and global radiation in Kuwait. Energy 60, 23–34.

Gordon, L.G., Leung, W., Johns, R., McNoe, B., Lindsay, D., Merollini, K.M., Elliott, T.M., Neale, R.E., Olsen, C.M., Pandeya, N., et al., 2022. Estimated healthcare costs of melanoma and keratinocyte skin cancers in Australia and Aotearoa New Zealand in 2021. Int. J. Environ. Res. Public Health 19 (6), 3178.

Gordon, L.G., Rowell, D., 2015. Health system costs of skin cancer and cost-effectiveness of skin cancer prevention and screening: a systematic review. Eur. J. Cancer Prev. 24 (2), 141–149.

Grandvalet, Y., Bengio, Y., 2004. Semi-supervised learning by entropy minimization. Adv. Neural Inf. Process. Syst. 17.

Hollósy, F., 2002. Effects of ultraviolet radiation on plant cells. Micron 33 (2), 179–197.

Holzinger, A., 2021. The next frontier: AI we can really trust. In: Joint European Conference on Machine Learning and Knowledge Discovery in Databases. Springer, pp. 427–440.

Holzinger, A., Dehmer, M., Emmert-Streib, F., Cucchiara, R., Augenstein, I., Del Ser, J., Samek, W., Jurisica, I., Díaz-Rodríguez, N., 2022. Information fusion as an integrative cross-cutting enabler to achieve robust, explainable, and trustworthy medical artificial intelligence. Inf. Fusion 79, 263–278.

Huang, L., Kang, J., Wan, M., Fang, L., Zhang, C., Zeng, Z., 2021. Solar radiation prediction using different machine learning algorithms and implications for extreme climate events. Front. Earth Sci. 9, 596860.

Igoe, D.P., Parisi, A.V., Downs, N.J., 2019. Cloud segmentation property extraction from total sky image repositories using Python. Instrum. Sci. Technol. 47 (5), 522–534.

Islam, M.J., Ahmad, S., Haque, F., Reaz, M.B.I., Bhuiyan, M.A.S., Islam, M.R., 2022a. Application of min-max normalization on subject-invariant EMG pattern recognition. IEEE Trans. Instrum. Meas. 71, 1–12.

Islam, M.S., Awal, M.A., Laboni, J.N., Pinki, F.T., Karmokar, S., Mumenin, K.M., Al-Ahmadi, S., Rahman, M.A., Hossain, M.S., Mirjalili, S., 2022b. Hgsorf: Henry gas solubility optimization-based random forest for C-section prediction and XAI-based cause analysis. Comput. Biol. Med. 147, 105671.

Jayasinghe, W.L.P., Deo, R.C., Ghahramani, A., Ghimire, S., Raj, N., 2022. Development and evaluation of hybrid deep learning long short-term memory network model for pan evaporation estimation trained with satellite and ground-based data. J. Hydrol. 607, 127534.

Jia, P., Cao, N., Yang, S., 2021. Real-time hourly ozone prediction system for Yangtze River Delta area using attention based on a sequence to sequence model. Atmos. Environ. 244, 117917.

Joseph, L.P., Deo, R.C., Casillas-Perez, D., Prasad, R., Raj, N., Salcedo-Sanz, S., 2024a. Multi-step-ahead wind speed forecast system: Hybrid multivariate decomposition and feature selection-based gated additive tree ensemble model. IEEE Access.

Joseph, L.P., Deo, R.C., Casillas-Pérez, D., Prasad, R., Raj, N., Salcedo-Sanz, S., 2024b. Short-term wind speed forecasting using an optimized three-phase convolutional neural network fused with bidirectional long short-term memory network model. Appl. Energy 359, 122624.

Joseph, L.P., Deo, R.C., Prasad, R., Salcedo-Sanz, S., Raj, N., Soar, J., 2023. Near real-time wind speed forecast model with bidirectional LSTM networks. Renew. Energy 204, 39–58.

Joseph, L.P., Joseph, E.A., Prasad, R., 2022. Explainable diabetes classification using hybrid Bayesian-optimized TabNet architecture. Comput. Biol. Med. 151, 106178.

Ketkar, N., Ketkar, N., 2017. Introduction to keras. In: Deep Learning with Python: a Hands-On Introduction. Springer, pp. 97–111.

Kuzlu, M., Cali, U., Sharma, V., Güler, Ö., 2020. Gaining insight into solar photovoltaic power generation forecasting utilizing explainable artificial intelligence tools. Ieee Access 8, 187814–187823.

Lan, H., Zhang, C., Hong, Y.-Y., He, Y., Wen, S., 2019. Day-ahead spatiotemporal solar irradiation forecasting using frequency-based hybrid principal component analysis and neural network. Appl. Energy 247, 389–402.

Lavker, R.M., Gerberick, G.F., Veres, D., Irwin, C.J., Kaidbey, K.H., 1995. Cumulative effects from repeated exposures to suberythemal doses of UVB and UVA in human skin. J. Am. Acad. Dermatol. 32 (1), 53–62.

Li, Z., 2022. Extracting spatial effects from machine learning model using local interpretation method: An example of SHAP and XGBoost. Comput. Environ. Urban Syst. 96, 101845.

Li, R., Guo, J., Geng, G., Xiao, Q., Zhang, Q., 2021. Satellite-derived long-term estimates of full-coverage PM1 concentrations across China based on a stacking decision tree model. Atmos. Environ. 255, 118448.

Li, W., Mo, W., Zhang, X., Squiers, J.J., Lu, Y., Sellke, E.W., Fan, W., DiMaio, J.M., Thatcher, J.E., 2015. Outlier detection and removal improves accuracy of machine learning approach to multispectral burn diagnostic imaging. J. Biomed. Opt. 20 (12), 121305–121305.

Luna, A., Paredes, M., De Oliveira, G., Corrêa, S., 2014. Prediction of ozone concentration in tropospheric levels using artificial neural networks and support vector machine at Rio de Janeiro, Brazil. Atmos. Environ. 98, 98–104.

Lundberg, S.M., Erion, G., Chen, H., DeGrave, A., Prutkin, J.M., Nair, B., Katz, R., Himmelfarb, J., Bansal, N., Lee, S.-I., 2020. From local explanations to global understanding with explainable AI for trees. Nat. Mach. Intell. 2 (1), 56–67.

Lyngdoh, G.A., Zaki, M., Krishnan, N.A., Das, S., 2022. Prediction of concrete strengths enabled by missing data imputation and interpretable machine learning. Cem. Concr. Compos. 128, 104414.

Ma, D., Xie, R., Pan, G., Zuo, Z., Chu, L., Ouyang, J., 2023. Photovoltaic power output prediction based on TabNet for regional distributed photovoltaic stations group. Energies 16 (15), 5649.

Madronich, S., Flocke, S., 1998. The role of solar radiation in atmospheric chemistry. In: Boule, P. (Ed.), Handbook of Environmental Chemistry. Springer-Verlag, pp. 1–26.

Malhi, A., Gao, R.X., 2004. PCA-based feature selection scheme for machine defect classification. IEEE Trans. Instrum. Meas. 53 (6), 1517–1525.

Martins, A., Astudillo, R., 2016. From softmax to sparsemax: A sparse model of attention and multi-label classification. In: International Conference on Machine Learning. PMLR, pp. 1614–1623.

Matsumura, Y., Ananthaswamy, H.N., 2004. Toxic effects of ultraviolet radiation on the skin. Toxicol. Appl. Pharmacol. 195 (3), 298–308.

McKenzie, R., Liley, B., Kotkamp, M., Geddes, A., Querel, R., Stierle, S., Lantz, K., Rhodes, S., Madronich, S., 2022. Relationahip between ozone and biologically relevant UV at 4 NDACC sites. Photochem. Photobiol. Sci. 21, 2095–2114.

mdVine, 2024. UniSQ atmoSEQ sensors. https://mdvine.atmoseq.cloud.edu.au/sensordata/. [Online]; (Accessed 18 July 2024].

Merlin, R.T., Ravi, R., 2023. RFECV and boruta: Advancing intrusion detection in iot and smart city networks. J. Namib. Stud.: Hist. Politics Cult. 38, 2015–2034.

Morris, V., 2005. Total sky imager (TSI) handbook. In: Atmospheric Radiation Measurement Rep. ARM TR-017.

Mulwa, M.M., Mwangi, R.W., Mindila, A., 2024. Gmm-LIME explainable machine learning model for interpreting sensor-based human gait. Eng. Rep. e12864.

Naik, J., Satapathy, P., Dash, P., 2018. Short-term wind speed and wind power prediction using hybrid empirical mode decomposition and kernel ridge regression. Appl. Soft Comput. 70, 1167–1188.

Notton, G., Voyant, C., Fouilloy, A., Duchaud, J.L., Nivet, M.L., 2019. Some applications of ANN to solar radiation estimation and forecasting for energy applications. Appl. Sci. 9 (1), 209.

Ochieng'Odhiambo, F., 2020. Comparative study of various methods of handling missing data. Math. Model. Appl. 5 (2), 87.

Olarte Saucedo, M., Sánchez Rodríguez, S.H., Arechiga Flores, C.F., Bañuelos Valenzuela, R., López Luna, M.A., 2019. Effects of ultraviolet radiation (UV) in domestic animals. Review. Revista Mexicana De Ciencias Pecuarias 10 (2), 416–432.

Ozgoren, M., Bilgili, M., Sahin, B., 2012. Estimation of global solar radiation using ANN over Turkey. Expert Syst. Appl. 39 (5), 5043–5051.

Ozoegwu, C.G., 2019. Artificial neural network forecast of monthly mean daily global solar radiation of selected locations based on time series and month number. J. Clean. Prod. 216, 1–13.

Pal, S., Sharma, P., 2021. A review of machine learning applications in land surface modeling. Earth 2 (1), 174–190.

Parisi, A.V., Downs, N., 2004. Cloud cover and horizontal plane eye damaging solar UV exposures. Int. J. Biometeorol. 49, 130–136.

Parker, E.R., 2021. The influence of climate change on skin cancer incidence–a review of the evidence. Int. J. Women's Dermatol. 7 (1), 17–27.

Pedregosa, F., Varoquaux, G., Gramfort, A., Michel, V., Thirion, B., Grisel, O., Blondel, M., Prettenhofer, P., Weiss, R., Dubourg, V., et al., 2011. Scikit-learn: Machine learning in Python. J. Mach. Learn. Res. 12, 2825–2830.

Piri, E., Babaeian, M., Tavassoli, A., Esmaeilian, Y., et al., 2011. Effects of UV irradiation on plants. Afr. J. Microbiol. Res. 5 (14), 1710–1716.

Prasad, S.S., Deo, R.C., Downs, N.J., Casillas-Pérez, D., Salcedo-Sanz, S., Parisi, A.V., 2024. Very short-term solar ultraviolet-A radiation forecasting system with cloud cover images and a Bayesian optimized interpretable artificial intelligence model. Expert Syst. Appl. 236, 121273.

Prasad, S.S., Deo, R.C., Downs, N., Igoe, D., Parisi, A.V., Soar, J., 2022. Cloud affected solar UV prediction with three-phase wavelet hybrid convolutional long short-term memory network multi-step forecast system. IEEE Access 10, 24704–24720.

Prasad, S.S., Deo, R.C., Salcedo-Sanz, S., Downs, N.J., Casillas-Pérez, D., Parisi, A.V., 2023. Enhanced joint hybrid deep neural network explainable artificial intelligence model for 1-hr ahead solar ultraviolet index prediction. Comput. Methods Programs Biomed. 241, 107737.

Premalatha, M., Naveen, C., et al., 2018. Analysis of different combinations of meteorological parameters in predicting the horizontal global solar radiation with ANN approach: A case study. Renew. Sustain. Energy Rev. 91, 248–258.

Qin, W., Wang, L., Wei, J., Hu, B., Liang, X., 2020. A novel efficient broadband model to derive daily surface solar Ultraviolet radiation (0.280–0.400 μm). Sci. Total Environ. 735, 139513.

Qing, X., Niu, Y., 2018. Hourly day-ahead solar irradiance prediction using weather forecasts by LSTM. Energy 148, 461–468.

Ribeiro, M.T., Singh, S., Guestrin, C., 2016. "Why should i trust you?" explaining the predictions of any classifier. In: Proceedings of the 22nd ACM SIGKDD International Conference on Knowledge Discovery and Data Mining. pp. 1135–1144.

Roth, A.E., 1988. The Shapley Value: Essays in Honor of Lloyd S. Shapley. Cambridge University Press.

Sabburg, J., Calbó, J., 2009. Five years of cloud enhanced surface UV radiation measurements at two sites (in the Northern and Southern) hemispheres. Atmos. Res. 93 (4), 902–912.

Sabburg, J., Long, C.N., 2004. Improved sky imaging for studies of enhanced UV irradiance. Atmos. Chem. Phys. 4, 2543–2552.

Salcedo-Sanz, S., Deo, R.C., Cornejo-Bueno, L., Camacho-Gómez, C., Ghimire, S., 2018. An efficient neuro-evolutionary hybrid modelling mechanism for the estimation of daily global solar radiation in the Sunshine State of Australia. Appl. Energy 209, 79–94.

Santamaría-Bonfil, G., Reyes-Ballesteros, A., Gershenson, C., 2016. Wind speed forecasting for wind farms: A method based on support vector regression. Renew. Energy 85, 790–809.

Sardashti, A., Nazari, J., 2023. A learning-based approach to fault detection and fault-tolerant control of permanent magnet DC motors. J. Eng. Appl. Sci. 70 (1), 109.

Sharaf, Z., Behzadifar, M., Behzadifar, M., Fitzmaurice, C., Abate, D., 2021. Global, regional, and National Cancer Incidence, mortality, years of life lost, years lived with disability, and disability-adjusted life-years for 29 cancer groups, 1990 to 2017. Glob. Burd. Cancer.

Sharma, E., Deo, R.C., Soar, J., Prasad, R., Parisi, A.V., Raj, N., 2022. Novel hybrid deep learning model for satellite based PM10 forecasting in the most polluted Australian hotspots. Atmos. Environ. 279, 119111.

Shi, K., Shi, R., Fu, T., Lu, Z., Zhang, J., 2024. A novel identification approach using RFECV–optuna–XGBoost for assessing surrounding rock grade of tunnel boring machine based on tunneling parameters. Appl. Sci. 14 (6), 2347.

Singh, S., Lodhi, N.K., Mishra, A.K., Jose, S., Kumar, S.N., Kotnala, R., 2018. Assessment of satellite-retrieved surface UVA and UVB radiation by comparison with ground-measurements and trends over Mega-city Delhi. Atmos. Environ. 188, 60–70.

Srinivas, P., Katarya, R., 2022. Hyoptxg: OPTUNA hyper-parameter optimization framework for predicting cardiovascular disease using xgboost. Biomed. Signal Process. Control 73, 103456.

Sterenborg, H., VanDerLeun, J., 1987. Action spectra for tumorigenesis by ultraviolet radiation. In: Human Exposure To Ultraviolet Radiation.

Tao, H., Jawad, A.H., Shather, A., Al-Khafaji, Z., Rashid, T.A., Ali, M., Al-Ansari, N., Marhoon, H.A., Shahid, S., Yaseen, Z.M., 2023. Machine learning algorithms for high-resolution prediction of spatiotemporal distribution of air pollution from meteorological and soil parameters. Environ. Int. 175, 107931.

Venugopal, K., Youlden, D., Te Marvelde, L., Meng, R., Aitken, J., Evans, S., Kostadinov, I., Nolan, R., Thomas, H., D'Onise, K., 2023. Twenty years of melanoma in Victoria, Queensland, and South Australia (1997–2016). Cancer Epidemiol. 83, 102321.

Villegas-Mier, C.G., Rodriguez-Resendiz, J., Álvarez-Alvarado, J.M., Jiménez-Hernández, H., Odry, Á., 2022. Optimized random forest for solar radiation prediction using sunshine hours. Micromachines 13 (9), 1406.

Vilone, G., Longo, L., 2021. Notions of explainability and evaluation approaches for explainable artificial intelligence. Inf. Fusion 76, 89–106.

Webb, A., Aseem, S., Kift, R., Rhodes, L., Farrar, M., 2016. Target the message: A qualitative study exploring knowledge and cultural attitudes to sunlight and vitamin D in Greater Manchester, UK. Br. J. Dermatol. 175 (6), 1401–1403.

Wong, P.-Y., Lee, H.-Y., Chen, Y.-C., Zeng, Y.-T., Chern, Y.-R., Chen, N.-T., Lung, S.-C.C., Su, H.-J., Wu, C.-D., 2021. Using a land use regression model with machine learning to estimate ground level PM2. 5. Environ. Pollut. 277, 116846.

World Health Organization, 2002. Global Solar UV Index: A Practical Guide. WHO, Geneva, Switzerland.